Ploypailin Kitrungrotjanaporn

Manuscript_B7_H2_Boiler (18.5.2026)

Somkid

Document Details

Submission ID

trn:oid:::3618:139706781

Submission Date

May 20, 2026, 3:30 PM GMT+7

Download Date

May 20, 2026, 3:35 PM GMT+7

File Name

Manuscript_B7_H2_Boiler (18.5.2026).pdf

File Size

9.0 MB

18 Pages

11,320 Words

58,595 Characters

8% Overall Similarity

The combined total of all matches, including overlapping sources, for each database.

Filtered from the Report

- Bibliography

Match Groups

44 Not Cited or Quoted 6%
Matches with neither in-text citation nor quotation marks

13 Missing Quotations 1%
Matches that are still very similar to source material

0 Missing Citation 0%
Matches that have quotation marks, but no in-text citation

0 Cited and Quoted 0%
Matches with in-text citation present, but no quotation marks

Top Sources

6% Internet sources
3% Publications
6% Submitted works (Student Papers)

Integrity Flags

0 Integrity Flags for Review

Our system's algorithms look deeply at a document for any inconsistencies that would set it apart from a normal submission. If we notice something strange, we flag it for you to review.

A Flag is not necessarily an indicator of a problem. However, we'd recommend you focus your attention there for further review.

Match Groups

- **44** Not Cited or Quoted 6%
  Matches with neither in-text citation nor quotation marks
- **13** Missing Quotations 1%
  Matches that are still very similar to source material
- **0** Missing Citation 0%
  Matches that have quotation marks, but no in-text citation
- **0** Cited and Quoted 0%
  Matches with in-text citation present, but no quotation marks

Top Sources

6% Internet sources
3% Publications
6% Submitted works (Student Papers)

Top Sources

The sources with the highest number of matches within the submission. Overlapping sources will not be displayed.

1 Internet
ijred.cbiore.id 2%

2 Student papers
Universitas Katolik Indonesia Atma Jaya on 2025-07-07 1%

3 Internet
mro.massey.ac.nz <1%

4 Student papers
Dr.Mahalingam college of engineering and technology on 2026-05-06 <1%

5 Publication
Aysel T. Atimtay, Ufuk Kayahan, Alper Unlu, Berrin Engin, Murat Varol, Hayati Olg... <1%

6 Publication
Nikolai V. Khartchenko, Vadym M. Kharchenko. "Advanced Energy Systems", CRC ... <1%

7 Student papers
University of Leeds on 2026-03-27 <1%

8 Internet
www.openveterinaryjournal.com <1%

9 Publication
Anaís Sánchez-Domínguez, Leticia del Carmen Ríos-Rodríguez, Jorge de la Torre y ... <1%

10 Publication
Ashish R. Kumar, Shimin Liu, Sekhar Bhattacharyya. "Mine Ventilation, Environm... <1%

11 Internet

bettercarenetwork.org <1%

12 Publication

Braem, Alan D., Jason T. Sweeney, and Jean W. Tom. "Process Scale-Up and Assess... <1%

13 Publication

Prapon Usirichun. "The photovoltaic boat for eco-tourism development in Koh Ra... <1%

14 Internet

journals.e-palli.com <1%

15 Publication

Hartmut Spliethoff. "Power Generation from Solid Fuels", Springer Nature, 2010 <1%

16 Student papers

University of Strathclyde on 2024-11-27 <1%

17 Internet

docplayer.biz.tr <1%

18 Internet

docs.cpuc.ca.gov <1%

19 Student papers

MyLearn on 2026-05-15 <1%

20 Student papers

Universitas Diponegoro on 2021-02-18 <1%

21 Publication

Zhongmin Wan, Jie Niu, Taiming Huang, Yuanli Liu, Yingkai Sun, Chen Yang, Yiyu ... <1%

22 Internet

doczz.biz.tr <1%

23 Internet

tel.archives-ouvertes.fr <1%

24 Publication

M. B. D. K. Siriwardena, Gamunu Samarakoon, Nabin Aryal, A. R. Nihmiya, Udara ... <1%

25 Publication

Masoud Lotfi Hejrandoost, Farivar Fazelpour, Alireza Saraei. "A new method to ov... <1%

26 Publication

Tiantian Wang, Hai Zhang, Yang Zhang, Hongjian Wang, Junfu Lyu, Guangxi Yue. "... <1%

27 Student papers

University of Leeds on 2025-02-25 <1%

28 Internet

ia800107.us.archive.org <1%

29 Internet

www.mdpi.com <1%

30 Internet

www.researchgate.net <1%

31 Publication

G. S. Marchenko, Anatolii Smikhula. "FEATURES OF COMBUSTION OF HYDROGEN ... <1%

32 Publication

Kaustubh Singh, Tikendra Nath Verma, Gaurav Dwivedi, Anoop Kumar Shukla. "H... <1%

33 Student papers

Universitas Trisakti FTKE-FTSP-FTI-FALTL-FH-FSRD on 2025-08-22 <1%

34 Student papers

University of Huddersfield on 2024-09-03 <1%

35 Student papers

Cranfield University on 2009-03-30 <1%

Contents list available at CBIORE journal website
International Journal of Renewable Energy Development
Journal homepage: https://ijred.cbiore.id
Research Article

Effect of Hydrogen Co-firing on Combustion Efficiency, Steam Production, and Emissions of a B7 Diesel Water-tube Boiler: An Experimental and Semi-empirical Combustion Modeling Study

Somkid Warasinchai[a] and Pongsakorn Kachapongkun[a*]

[a]Rattanakosin College for Sustainable Energy and Environment, Rajamangala University of Technology Rattanakosin (RMUTR), Thailand
*Corresponding author: pongsakorn.kerd@rmutr.ac.th

List of ORCID of each author
Somkid Warasinchai: https://orcid.org/0009-0000-0672-4139
Pongsakorn Kachapongkun: https://orcid.org/0000-0002-6902-0187

Abstract

Hydrogen co-firing is a near-term decarbonization option for industrial steam boilers in Southeast Asia, where B7 diesel (a 7% palm-oil FAME blend) is the mandated fuel, yet experimental evidence in this class of equipment remains limited. We report a controlled experimental campaign on a 1,000 kg/hr water-tube boiler (Kawasaki 15750) at H_2/diesel energy ratios from 0 to 30%, with four steady-state replicates per condition. We interpret these measurements with a calibrated PSR/PFR combustion model with extended Zeldovich NO_x kinetics and a 2D axisymmetric CFD simulation. At 30% H_2, steam output rose 24.3% (323.8 → 402.4 kg/hr) with diesel feed held constant; combustion air was trimmed by supplemental O_2 to hold stoichiometry roughly constant as the H_2 ratio climbed (contributing ~10–15% of the NO_x rise). CO_2 intensity per kg steam fell 20.1% (202.5 → 161.9 g/kg), CO dropped 73.2% (106.5 → 28.5 ppmv), and estimated NO_x rose ~64% (NO_2-derived; see §2.3), consistent with thermal-NO_x amplification. System efficiency (ASME PTC 4.1 Direct Method) peaked at 93.42% near 5% H_2 and declined to 87.45% at 30% H_2. Second-order polynomial correlations (Eqs. 6–9, $R^2 \approx 0.96–0.99$) give compact screening rules, and the CFD model reproduced the measured trends. A fuel-cost-only sensitivity at 2026 Thai market prices (excluding capital, storage, and safety costs) puts the fuel-cost-favorable window at about 12% H_2; under the IRENA Green Hydrogen trajectory, this window expands to the full 0–30% range by 2030. At low-fire operation, H_2 co-firing is a practical retrofit option for B7 diesel water-tube boilers, with NO_x as the principal trade-off.

Keywords: B7 biodiesel; Boiler efficiency; Boiler retrofit; CO reduction; Combustion emissions; Hydrogen co-firing; NO_x; Semi-empirical combustion model; Steam production; Water-tube boiler

Received: xxx; Revised: xxxx; Accepted: xxx; Available online: xxx

1. Introduction

About a fifth of global final energy still goes to industrial heat, and most of it is still produced by burning fossil fuel, as reported by the International Renewable Energy Agency (IRENA, 2024). That makes industrial heat a stubborn target for the kind of emissions reductions called for by Paris-aligned policy, per the International Energy Agency (IEA, 2023, Energy Policy and Planning Office, 2023). Industrial heat in Southeast Asia is still dominated by fossil fuels (IEA, 2024), and water-tube boilers carry much of that load in food processing, textiles, chemicals, and palm-oil milling, where they are a recognized source of CO, NO_x, SO_2, and CO_2. Thai industry runs on B7 diesel, a 7% v/v palm-oil FAME blend mandated by the Ministry of Energy (Department of Energy Business, 2020), and water-tube boilers in the 0.5–5 MW thermal range supply most of the country's industrial steam (Energy Policy and Planning Office et al., 2021, Department of Industrial Works, 2024).

Co-firing hydrogen with the existing fuel, as opposed to a full conversion to H_2, is appealing because it uses the boiler hardware already in place. Burner replacement and major control rework are largely avoided at low-to-moderate blending ratios, so the up-front cost is contained (Capurso et al., 2022). Hydrogen also brings combustion properties that suit boiler service: a flammability range of 4–75 vol.%, a laminar flame speed near 2.9 m/s versus roughly 0.30 m/s for diesel, and no direct CO_2 at the point of combustion (Turns, 1996, NASA, 1997). Recent reviews of hydrogen as an alternative fuel in combustion systems have summarized its clean-combustion characteristics, the engine and burner modifications required, and the economic and safety challenges that still constrain widespread deployment (Long Huynh et al., 2024). Most of that synthesis, however, has been built around internal-combustion-engine applications, with comparatively little quantitative evidence on liquid-fuel industrial boilers — and even less on diesel-biodiesel blends such as B7.

The literature on H_2 co-firing in liquid-fuel industrial boilers is sparse. Most of the published experimental work has been on H_2–natural gas blends, either in domestic appliances (Boulahlib et al., 2021, Gersena et al., 2020) or in industrial gas turbines (Laget et al., 2023), where the baseline chemistry is unlike that of distillate liquid fuels. Biodiesel–H_2 work has concentrated on compression-ignition engines (Periyathambi et al., 2025, Jayabal and Sivanraju, 2025). In a broader survey of dual-fuel diesel engines, Hosseini et al. (2023) reported the same pattern across the literature — CO, unburned hydrocarbons, and particulates all decrease with H_2 admission, while NO_x rises because of the higher in-cylinder temperatures, with engine performance gains plateauing near 30% H_2 on an energy basis. The combustion mechanisms they describe — faster radical-pool development, shorter ignition delay, and leaner local flame zones — should carry over qualitatively to a diesel-fired boiler, even though boiler flames are non-premixed and operate at lower peak temperatures than engine cycles. Khiraiya et al. (2021) and Lin and Wu (Lin and Wu, 2023) tested biodiesel blends (B5–B100) in an experimental boiler but did not include hydrogen. More recent work on hydrogen-enriched industrial burners and boilers (Lan et al., 2024, Wang et al., 2022, Nemitallah et al., 2024) reports NO_x trends consistent with a thermal mechanism. Sun et al. (2024) reported the same efficiency-NO_x trade-off in a 2 t/h gas boiler. Xin et al. (2021) modeled the heat-release shift via CFD at 200 kW. Schwarz et al. (2024) reported a 16.3% rise in load-cooling capacity in oxy-fuel mode. The boiler/biodiesel pairing, however, has barely been touched. Quantitative data on what H_2 enrichment does, simultaneously, to combustion chemistry, steam productivity, and thermal efficiency in a B7-fired industrial boiler are essentially missing. A summary of the H_2/fuel ratios reported in this body of work, set against the present study, is given in Table 1.

Ref	Study / System	Method	Primary fuel	H_2 range	Key finding
(Boulahlib et al., 2021)	**Boulahlib et al. 2021** — domestic boiler, 15 kW (16-burner).	Experimental	CH_4	0–45 vol.%	+1.2% combustion efficiency and −16% CO_2 at 40% H_2; optimum at 20% H_2 with fuel-rich staging factor 2.0.
(Gersena et al., 2020)	**Gersena et al. 2020** — domestic NG/H_2 boiler system.	Experimental + System development	Natural gas	up to ~30 vol.%	System-level development of a residential H_2-blend boiler.
(Laget et al., 2023)	**Laget et al. 2023** — industrial gas turbine, 24 MW (Siemens SGT-600)	Experimental (industrial demonstration)	Natural gas	0–25 vol.%	Stable operation across base/part load; NO_x and combustion dynamics monitored.
(Lan et al., 2024)	**Lan et al. 2024** — NG industrial heating furnace.	Experimental + CFD	Natural gas	0–30 vol.% (4 mixtures)	Progressive CO reduction with H_2; OH-mediated burnout dominant.
(Wang et al., 2022)	**Wang et al. 2022** — industrial steam boiler, 108 t/h.	Experimental (case study)	Natural gas	0–90 vol.%	Trade-off between thermal efficiency and NO_x; quantified decarbonization potential.
(Nemitallah et al., 2024)	**Nemitallah et al. 2024** — industrial water-tube boiler, 207 MW.	Experimental (retrofit)	Natural gas	0–100 vol.%	Identified hardware modifications required; NO_x rises sharply at low H_2 and stabilizes above 30%.
(Sun et al., 2024)	**Sun et al. 2024** — gas-fired steam boiler, 2 t/h (WNS2-1.25-Q).	Numerical (kinetic modeling) + Experimental (field test)	Natural gas	0–25 vol.%	CHEMKIN PRO (PREMIX + OPPDIF) for kinetics + on-site field test; trade-off between thermal efficiency and NOx emission as H_2 ratio rises.
(Xin et al., 2021)	**Xin et al. 2021** — casing swirl burner gas boiler, 200 kW.	CFD	Natural gas	0–100 vol.% (6 conditions)	CFD with constant power and constant excess air; H_2 increases peak temperature, accelerates combustion rate, reduces CO_2 and total flue gas, and inhibits NOx and soot under their fixed-stoichiometry constraint.
(Schwarz et al., 2024)	**Schwarz et al. 2024** — semi-industrial oxy-fuel burner, 100–140 kW.	Experimental	Natural gas (O_2 enriched)	0–100 vol.%	Pure-H_2 lowers flue-gas T by 126 K and raises load-cooling capacity by 16.3% at constant fuel energy; heat-transfer shifts toward more convective load.

ISSN: 2252-4940/© xxx. The Author(s). Published by CBIORE

Ref	Study / System	Method	Primary fuel	H_2 range	Key finding
(Glanville et al., 2022)	**Glanville et al. 2022** — partially premixed combustion equipment.	Experimental	Natural gas	0–30 vol.%	Reliable operation up to 30% H_2 with minor performance changes; consistent NO_x rise.
This study	B7 diesel water-tube boiler, 1,000 kg/hr (Kawasaki 15750, low-fire).	Experimental + Semi-empirical correlation + CFD	B7 diesel	0–30% H_2/diesel energy	+24.3% steam at 30%; −20.1% CO_2/kg steam; −73.2% CO emission; +64.0% NO_x; system efficiency declines 3.6 pp (ASME PTC 4.1 Direct Method).

Table 1. H_2 blending ratios reported in the recent literature on hydrogen co-firing in industrial combustion systems, set against the present study.

Our work targets part of that gap directly. We ran a controlled experimental campaign on a commercial 1,000 kg/hr-class vertical water-tube boiler (Kawasaki 15750, low-fire, saturated steam at 0 barg) and supplemented it with a calibrated semi-empirical combustion model. We set out to quantify the effect of H_2/diesel energy ratios from 0 to 30% on CO, NO_x, CO_2, SO_2, flue-gas temperature, and net thermal efficiency; to measure how much extra steam capacity the H_2 unlocks; to fit polynomial correlations for key performance indicators in the tested operating window; and to read off what the economics and emissions picture means for operators considering H_2 co-firing as a decarbonization step.

Relation to prior reporting. A portion of the underlying experimental dataset (Table 4 measurements at the seven H_2/diesel energy ratios) has been previously reported in the Thai-language preliminary paper by Warasinchai and Kachapongkun (Warasinchai and Kachapongkun, 2026), which presents only the basic experimental observations without the combustion modeling, CFD simulation, polynomial correlations, economic sensitivity analysis, or lifecycle CO_2 assessment developed in the present manuscript. The two manuscripts share the same experimental campaign but address substantially different audiences and depths of analysis. The present paper extends the Thai preliminary report with: (i) a calibrated semi-empirical PSR/PFR combustion model with extended Zeldovich NO_x kinetics; (ii) a 2D axisymmetric CFD model validated against the experiments; (iii) polynomial regression correlations for engineering use (Eqs. 6–9); (iv) a multi-scenario economic sensitivity analysis using the IRENA Green Hydrogen Cost Reduction trajectory; and (v) a quantitative lifecycle CO_2 comparison across gray, blue, and green hydrogen pathways.

2. Materials and Methods

2.1 Boiler System and Test Configuration

Experiments were conducted on a vertical water-tube boiler (Kawasaki 15750) rated at 1,000 kg/hr saturated steam at 0 barg (100 °C, h_g ≈ 2,676 kJ/kg for dry saturated; actual delivered steam at x ≈ 0.95 — see §2.3), operated at the low-fire setting (~870 MJ/hr) throughout. The pressure-atomizing oil burner runs on B7 diesel; a hydrogen injection port was installed upstream of the air inlet for H_2 premixing with combustion air. H_2 at ≥99.6% purity was supplied from 2,500 psi (≈172 bar) cylinders and regulated to 5 bar at the injection port; supplemental O_2 (≥99.5%, 150 bar cylinders regulated to 5 bar) was added to the combustion air. The O_2 assist was needed because the air-to-fuel ratio at low-fire on B7 sits close to the lean stability limit. Rather than fix the O_2 flow, the excess-air level in the flue gas was tracked continuously and O_2 supply was trimmed upward as H_2 ratio increased, keeping excess-air constant across all seven conditions; differences between conditions therefore come from the H_2 chemistry rather than from air-supply shifts. A caveat: the supplemental O_2 raises local O_2 partial pressure above what an air-only flame would experience; an ancillary CFD sensitivity attributes ~10–15% of the estimated +~64% NO_x rise at 30% H_2 to the O_2-enrichment temperature lift, with the remaining ~85% attributable to H_2 kinetics. The overall experimental layout is shown in Fig. 1.

Hydrogen safety was a major concern. H_2 has a wide flammability range (4–75 vol.% in air) and low minimum ignition energy (MIE ≈ 0.017 mJ vs ~0.25 mJ for methane). Certified flash-back arresters were fitted at H_2/O_2 regulator outlets and injection-port inlets; injection pressure was held below 0.5 barg to prevent reverse flow. Two H_2-specific electrochemical leak detectors monitored the area with audible alarms, and continuous forced ventilation was maintained throughout. Hydrogen handling followed NFPA 2 and Thai DIW safety practice for compressed-gas operations.

Fuel use was tracked gravimetrically with a calibrated platform scale (±0.001 kg) at the B7 day tank. Steam and feedwater flow were derived from sequential turbine water-meter readings (±0.5 kg/hr) over each timed interval. Hydrogen flow was set and measured with a calibrated rotameter (calibrated for H_2, ±2% FS) running at atmospheric pressure and ambient temperature, and the volumetric reading was converted to mass flow using H_2 density at the measured ambient conditions. For each target energy ratio, the volumetric set-point was pre-calculated from Eq. 2 using the measured diesel rate and the known LHVs; the rotameter was opened to that reading and held for the rest of the test. Combined uncertainty of the H_2 energy fraction is estimated at about ±3 percentage points of the nominal ratio.

Uncertainty of the derived H_2 energy fraction r was estimated by error propagation: δr/r = √[(δṁ_H_2/ṁ_H_2)² + (δLHV_B7/LHV_B7)²], with δṁ_H_2/ṁ_H_2 = ±2% (rotameter full-scale calibration) and δLHV_B7/LHV_B7 ≈ ±0.3% (blend rule). The rotameter dominates the budget, giving a propagated relative uncertainty of about ±2.1%, or roughly ±0.6 percentage points at r = 30%. The ±3 pp figure quoted above is therefore deliberately conservative and absorbs the manual valve-setting error on top. That level of uncertainty is typical for rotameter-based flow measurement in industrial H_2 co-firing tests and does not change any of the qualitative conclusions.

At the B7-only baseline, the Testo 350 reported a residual flue-gas H_2 concentration of ~26.75 ppm. The reading was stable across the four replicates (CV < 2%) and is most plausibly a combination of trace H_2 from partial thermal cracking of B7 in the primary zone ($C_nH_m + H_2O \rightarrow CO + H_2$) and known cross-

ISSN: 2252-4940/© xxx. The Author(s). Published by CBIORE

sensitivity of the electrochemical H_2 cell to unsaturated hydrocarbons (ethylene, acetylene) common in biodiesel combustion. Because the residual H_2 in the flue gas is a negligible fraction of the H_2 injected at any non-zero condition (ppm in the flue versus kg/hr at the rotameter), the rotameter set-point was the primary basis for setting the energy ratio.

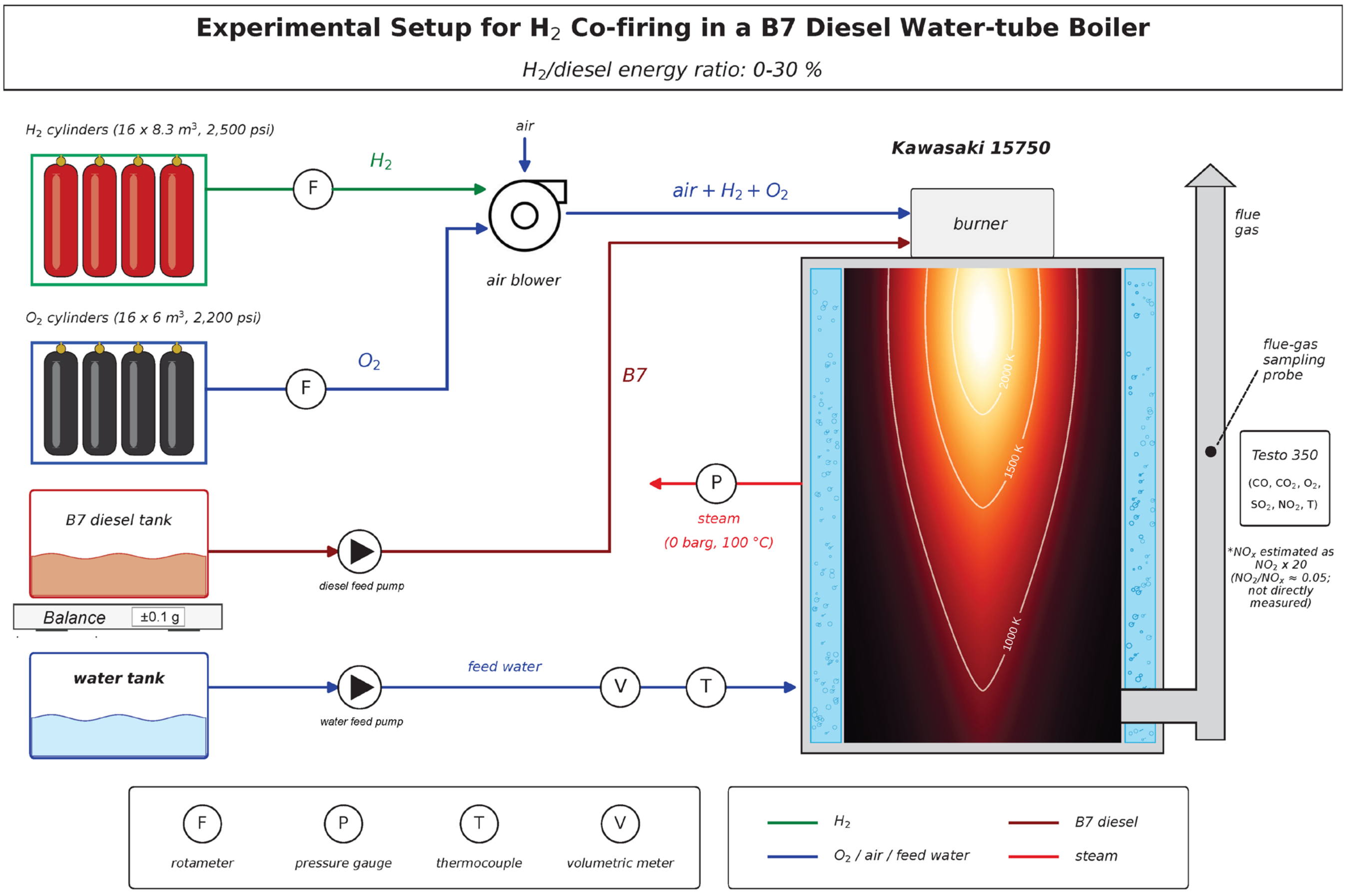

Fig. 1. Schematic of the experimental setup for hydrogen co-firing in a B7 diesel water-tube boiler (Kawasaki 15750). B7 diesel is delivered gravimetrically from a day tank on an electronic balance (±0.1 g) through a diesel feed pump to the burner. Premixed H_2 (16-cylinder bank, 8.3 ft³ × 2,500 psi each) is metered through a rotameter (FR) and supplemental O_2 through a flowmeter (F) into the air blower, which also draws ambient air; the premixed air + H_2 + O_2 stream enters the combustion chamber. Saturated steam exits at 0 barg (red arrow; pressure gauge P); feed water flow is monitored by volumetric (V), thermocouple (T), and flow (F) instruments. Combustion products exit via the stack, where a Type-K thermocouple and flue-gas sampling probe feed a Testo 350 portable analyser (CO, CO_2, O_2, SO_2, NO_2, flue-gas temperature). Lines and instruments are not to scale.

2.2 Fuel Properties

The B7 diesel used here meets the Thai Ministry of Energy standard (TIS 1267-2556): 93 vol.% fossil diesel and 7 vol.% palm-oil FAME (Department of Energy Business, 2020). For modeling we adopted the surrogate $C_{12\cdot5}H_{22\cdot1}O_{0\cdot2}S_{0\cdot002}$ (MW = 170.7 g/mol). The lower heating value comes from the blend rule $LHV^{B}{}_{7}$ = 0.93×43.0 + 0.07×37.5 = 42.62 MJ/kg. Hydrogen LHV was set to the standard value of 119.96 MJ/kg, as standardized by the National Aeronautics and Space Administration (NASA, 1997). Table 2 lists the fuel properties used throughout the study.

Property	B7 Diesel	Hydrogen	Unit
Lower Heating Value (LHV)	42.62	119.96	MJ/kg
Density (at 15 °C)	0.840	0.0838	kg/L / kg/m³ (STP)
Molecular formula (surrogate)	$C_{12\cdot5}H_{22\cdot1}O_{0\cdot2}S_{0\cdot002}$	H_2	—
Molecular weight (surrogate)	170.7	2.016	g/mol
Stoich. O_2 requirement	13.62	7.94	kg O_2/kg fuel
Adiabatic flame temp. (λ = 1.0)	~2363	~2385	K
Laminar flame speed	~0.4	~2.9	m/s

Table 2. Fuel properties of B7 diesel and hydrogen used in this study.

2.3 Measurement System and Instrumentation

Flue-gas composition was monitored continuously with a portable electrochemical analyzer (Testo 350) inserted into the flue-gas stack. The analyzer logged O_2 (%), CO (ppm), NO_2 (ppm), CO_2 (%), SO_2 (ppm), flue-gas temperature (°C), and residual H_2 (ppm) on a dry basis, with the sample dried by a built-in desiccant. Total NO_x was estimated by multiplying the measured NO_2 by 20 (i.e., assuming a fixed NO_2/NO_x fraction of

ISSN: 2252-4940/© xxx. The Author(s). Published by CBIORE

5%), which is consistent with the NO-dominated speciation typical of diesel combustion at moderate temperature (Correa, 1993, EPRI, 2020). Direct NO measurement was not available on this instrument, and the 5% assumption is a fixed engineering approximation that can shift with temperature and excess air. The reported NO_x values are best read as engineering estimates, and we treat the limitation explicitly later in this section. Direct NO speciation is on our list of recommended next steps.

To check how sensitive the NO_x numbers are to the f assumption, we re-ran the conversion with three values: f = 5% (this study), f = 6.5% (representative of gas-turbine combustion at moderate excess air (Wang and Yang, 2024)), and f = 8% (a conservative upper bound for oxygen-enriched, high-temperature conditions (Glarborg et al., 2018, Pan et al., 2023)). Across the measured NO_2 range of 1.70–3.08 ppm, the estimated NO_x comes out at 37.5–61.5 ppm at f = 5%, 26.7–47.3 ppm at f = 6.5%, and 21.7–38.4 ppm at f = 8%. The monotonically rising NO_x trend survives all three assumptions, but the absolute level moves substantially. The percentage change of 64.0% is identical under any choice of f, since it depends only on the ratio of NO_2 readings. The f-dependent magnitude is the reason direct NO measurement is listed as a key future-work recommendation in Section 4.

A second caveat: the Testo 350 NO_2 cell carries a declared accuracy of ±5 ppm, but the measured NO_2 values (1.70–3.08 ppm) sit below that bound, so individual readings may be inside the sensor noise floor. The internal consistency (monotonic rise across n = 4 replicates per condition) gives qualitative confidence in the upward trend with H_2 ratio. Propagating the Testo 350 NO_2 accuracy (±5 ppm) through Eq. 3 with f = 0.05 ± 0.015 yields a combined relative uncertainty of ~±70% on absolute NO_x; only the monotonically increasing trend (estimated NO_x ~1.6× at r = 0.30 relative to baseline) is reliably resolved by the measurements. Absolute NO_x values should be interpreted as semi-quantitative engineering estimates rather than measurement-grade quantities.

Boiler efficiency was computed using the Direct Method per ASME PTC 4.1 (Steam Generating Units Performance Test Code) by the American Society of Mechanical Engineers (ASME, 2013). Efficiency is the ratio of useful heat output to fuel heat input:

$$\eta = [\dot{m}\_st \times (h\_f + x \cdot h\_fg - h\_fw)] / [\dot{m}\_fuel \times LHV\_fuel] \times 100\% \quad (Eq. 1)$$

Here ṁ_st is saturated steam mass flow (kg/hr), h_f = 419 kJ/kg and h_fg = 2,257 kJ/kg are the saturated-liquid enthalpy and latent heat of vaporization at 0 barg (100 °C), x = 0.95 is the steam quality at the boiler outlet (industry-standard value for industrial water-tube boilers without integral dryer/superheater (Stultz and Kitto, 2005); cross-checked against the Testo 350 Indirect combustion efficiency of ~92.5% across all conditions — the ~1.5 percentage-point gap to the reported Direct efficiency represents radiation/convection losses typical for industrial boilers operating below rated capacity (Çengel et al., 2019), h_fw ≈ 125.8 kJ/kg is feedwater enthalpy at ~30 °C, ṁ_fuel is total fuel flow (B7 + H_2, kg/hr), and LHV_fuel is the blended lower heating value (kJ/kg). At every test condition the boiler was first allowed to settle for approximately 25 minutes, after which six to nine flue-gas readings were logged at five-minute intervals during the validated steady-state window. To maintain a consistent sample size, the readings were sorted and the extreme values were trimmed symmetrically from each end until four remained (i.e., the central n = 4 per condition), following the protocol designed via statistical power analysis (β = 0.80, moderate effect size). Any transient readings (e.g., burner ramp-down at the end of a run) were excluded before trimming. The sample size is adequate given the very large effect sizes observed ($\eta^2 \approx 0.98$, statistical power > 0.999). A sensitivity check using all six (untrimmed) readings produced condition means within 0.3% of the trimmed values, confirming that the exclusion criterion does not drive the conclusions; full untrimmed mean and SD per condition are reported in the Supplementary Material. From the four retained readings, the condition mean, SD, SEM, and 95% CI (= 1.96 × SEM) were computed. The coefficient of variation for net efficiency stayed below 0.07% across all conditions, confirming good repeatability.

Boiler efficiency reported throughout is the System Efficiency from Eq. 1 (ASME PTC 4.1 Direct Method) using measured steam flow, feedwater enthalpy, and total fuel mass flow with both fuel streams in the energy denominator. Defining energy input on a total-fuel basis is essential when H_2 co-firing supplies a non-negligible share of heat input. The Testo 350 also reports an Indirect (loss-based) Net efficiency from flue-gas composition alone (~92.5% across conditions); this is not used here because it overestimates system efficiency at higher H_2 ratios where heat-transfer-limited losses appear (see §3.6).

2.4 Experimental Conditions

We ran seven conditions corresponding to H_2/diesel energy ratios of 0, 5, 10, 15, 20, 25, and 30%. The ratio is defined as:

$$r = (\dot{m}\_H_2 \times LHV\_H_2) / (\dot{m}\_B7 \times LHV\_B7) \quad (Eq. 2)$$

Under this definition, an r value of 0.30 corresponds to hydrogen supplying 23.1% of the total fuel energy input. The total-energy fraction is f = r/(1+r); at r = 0.30, f = 0.231. The diesel feed was held essentially constant across all conditions, in the range 20.25–20.52 kg/hr (CV < 0.6%). Hydrogen therefore acted as an add-on fuel, not as a substitute for diesel. To minimize day-to-day drift, all seven conditions were tested on the same calendar day, 12 September 2025. The ambient temperature during the campaign ranged between 31.8 and 33.3 °C. The resulting operating conditions, instrumentation readings, and steady-state averages are listed in Table 3.

H_2/Diesel Ratio (%)	Diesel Rate (kg/hr)	H_2 Flow (kg/hr)	Steam Rate (kg/hr)	Diesel Heat Input (MJ/hr)	System Eff. (%)	n (readings)
0	20.36	0.000	323.8	867.6	91.05 ± 0.05	4
5	20.30	0.361	348.0	865.3	93.42 ± 0.05	4
10	20.31	0.722	363.8	865.6	93.18 ± 0.05	4
15	20.52	1.094	368.6	874.8	89.47 ± 0.05	4

ISSN: 2252-4940/© xxx. The Author(s). Published by CBIORE

H_2/Diesel Ratio (%)	Diesel Rate (kg/hr)	H_2 Flow (kg/hr)	Steam Rate (kg/hr)	Diesel Heat Input (MJ/hr)	System Eff. (%)	n (readings)
20	20.31	1.443	384.4	865.5	90.23 ± 0.05	4
25	20.25	1.798	397.1	862.9	89.68 ± 0.05	4
30	20.22	2.155	402.4	861.6	87.45 ± 0.05	4

Table 3. Experimental conditions and operational parameters (mean ± SD; n = 4 steady-state replicates per H_2 ratio). System efficiency follows ASME PTC 4.1 Direct Method (Eq. 1).

2.5 Semi-empirical Combustion Model

To frame the experimental data physically, we built a lumped-parameter semi-empirical combustion model. The framework has three coupled sub-models.

(a) Adiabatic flame temperature (T_ad). T_ad is computed from an energy balance over the combustion products at stoichiometric composition, using mean molar heat capacities evaluated at 1,200 K for CO_2 (54.3 J/mol/K), H_2O (39.3), O_2 (32.7), N_2 (31.1), and SO_2 (51.1). The excess-air ratio λ is back-calculated from the measured flue-gas O_2.

(b) NO_x formation. Thermal NO_x uses the extended Zeldovich mechanism (Turns, 1996) driven by the computed T_ad, with an OH-enhancement term added to capture the well-documented effect of H_2 enrichment:

$$NO_x = k\_scale \times \exp(-38370/T\_ad) \times [O_2]^{0.5} \times [N_2] \times \tau \times (1 + \beta \cdot r) \qquad \text{(Eq. 3)}$$

k_scale is a single calibration constant fit to the baseline (r = 0) measurement, τ = 0.50 s is the estimated reactor residence time, and β = 1.93 is the OH-enhancement coefficient obtained by least-squares calibration of Eq. 3 to the measured NO_x trend across all seven H_2/diesel ratios (β captures the combined response of the Arrhenius, $[O_2]$^0.5, $[N_2]$, and residence-time terms; it does not reduce to a simple two-point ratio).

(c) CO burnout and boiler efficiency. CO burnout in the post-flame zone uses the Dryer–Glassman rate expression (Dryer and Glassman, 1973) in a PFR configuration. Boiler efficiency in the model uses the same ASME PTC 4.1 Direct Method as above (Eq. 1), with wet-steam enthalpy at 0 barg (x = 0.95) and feedwater enthalpy at the measured inlet temperature. Calibration was done on the baseline (0% H_2) data and no further fitting parameters were used for the rest of the conditions.

2.6 Two-Dimensional Axisymmetric CFD Model

To get a spatially resolved view to go alongside the lumped model, we built a 2D axisymmetric CFD of the Kawasaki 15750 (1,000 kg/hr rated, low-fire, 0 barg). Detailed three-dimensional CFD coupled with solid-mechanics has been applied to hydrogen-fueled combustion components such as piston crowns to capture localized thermomechanical loads and stress distributions (Al-Baghdadi et al., 2023). For the present industrial-scale boiler — operating at steady state with axisymmetric burner geometry firing downward into a vertical water-tube bundle — a 2D axisymmetric reduction captures the dominant flame and emission characteristics at substantially lower computational cost while remaining consistent with the model's intended use as a screening tool. The computational domain extends over an axial length of L = 1.5 m and a radial extent of R_n = 0.35 m, corresponding to the inner combustion chamber dimensions of the Kawasaki 15750 unit; the burner radius is r_burner = 0.045 m at the inlet. The governing equations are written in the parabolic form appropriate for confined reacting flows with axial bulk convection and radial diffusion:

$$\rho u\, \partial T/\partial z = (1/r)\partial/\partial r(r\lambda\_eff\, \partial T/\partial r) + S\_T \qquad \text{(Eq. 4a)}$$

$$\rho u\, \partial Y\_i/\partial z = (1/r)\partial/\partial r(r\rho D\_i\, \partial Y\_i/\partial r) + S\_i \qquad \text{(Eq. 4b)}$$

The effective conductivity is λ_eff = λ_mol + λ_t with Pr_t = 0.70. The axial velocity u is taken as uniform plug flow at u ≈ 4 m/s. Boundary conditions are symmetry (∂ϕ/∂r = 0 at r = 0) and T_wall = 500 K at r = R_n (inner wall of the water tubes). Combustion heat release S_T is represented by a Gaussian profile (Law, 2006) centered on the burner quarl and confined to z < 1.5 z_flame.

Mesh independence. Three grids were compared (coarse 20×50, baseline 35×80, fine 50×120); exit-plane CO and NO_x changed by <2.1% between baseline and fine. The baseline grid (35×80) was used for production runs. Full mesh-convergence data are reported in the Supplementary Material.

Turbulence closure. Mixing-length closure (ℓ_m = 0.09 *D_n*, *Pr_t* = 0.70) was used, consistent with the parabolic plug-flow assumption and the exit-plane integral focus of the model. Justification and alternatives are summarized in the Supplementary Material.

Species sub-models. CO burnout follows the Dryer–Glassman expression (Eq. 5) in the post-flame zone, mirroring the 0-D model. NO_x formation uses the extended Zeldovich mechanism with the same OH-enhancement coefficient β = 1.93 above 1,400 K:

$$-d[CO]/dt = A \exp(-E\_a/RT)[CO][H_2O]^{0.5}[O_2]^{0.25} \qquad \text{(Eq. 5)}$$

The system is discretized on a non-uniform N_r = 35 × N_z = 80 grid and solved by marching in z with an implicit Thomas (tridiagonal) algorithm at each axial station. Area-weighted exit-plane averages are compared directly with the seven experimental conditions (n = 4 each). The model is implemented in Python 3 using NumPy and the source code is provided as supplementary material.

3. Results and Discussion

3.1 Combustion Emissions Overview

Table 4 collects the experimental results for every measured parameter and operating variable. Values are mean ± standard deviation, with 95% CIs given for the key outputs. Repeatability across the seven conditions was good: efficiency CV stayed under 0.07% and CO_2 CV under 1.0%, in line with the trimming protocol and the quasi-steady operation.

ISSN: 2252-4940/© xxx. The Author(s). Published by CBIORE

H_2 (%)	CO (ppm)	NO_x (ppm, est.)	CO_2 (%)	SO_2 (ppm)	T_flue (°C)	System Eff. (%)
0	106.5 ± 11.7	37.5 ± 1.0	12.90 ± 0.03	0.25 ± 0.50	193.4 ± 0.3	91.05 ± 0.05
5	70.2 ± 6.7	46.0 ± 1.6	13.34 ± 0.06	0.50 ± 0.58	194.1 ± 0.3	93.42 ± 0.05
10	58.2 ± 6.6	50.0 ± 0.0	13.52 ± 0.02	0.25 ± 0.50	193.5 ± 0.1	93.18 ± 0.05
15	46.8 ± 4.2	52.0 ± 1.6	13.70 ± 0.03	0.00 ± 0.00	193.9 ± 0.1	89.47 ± 0.05
20	41.8 ± 3.3	54.5 ± 1.0	13.79 ± 0.05	0.00 ± 0.00	194.2 ± 0.4	90.23 ± 0.05
25	38.0 ± 2.2	57.5 ± 1.0	13.96 ± 0.03	0.00 ± 0.00	196.4 ± 0.1	89.68 ± 0.05
30	28.5 ± 1.7	61.5 ± 1.0	14.07 ± 0.03	0.00 ± 0.00	197.2 ± 0.0	87.45 ± 0.05

Table 4. Experimental results: mean ± SD for key combustion parameters (n = 4 steady-state replicates per condition; boundary readings excluded following the stabilization criteria). NO_x = NO_2(measured) × 20.

† NO_x (ppm, est.): estimated from NO_2(measured) × 20, assuming a fixed NO_2/NO_x fraction of 5%. See Section 2.3 for the sensitivity analysis. The ±1.0 ppm uncertainty shown in the table reflects replicate-to-replicate variation only; the absolute uncertainty including sensor accuracy is ~±70% (see §2.3). The monotonically increasing trend is reliably resolved, but absolute magnitudes should be read as semi-quantitative engineering estimates.

‡ CO_2 (%): dry-basis concentration measured after desiccant dehumidification. The reported values are higher than the true wet-basis composition because removing H_2O concentrates the dry-gas species. The apparent CO_2 rise with H_2 ratio is therefore a measurement artifact, not a real increase in carbon output per unit fuel; see Section 3.5 for the full discussion.

The SO_2 readings in Table 4 deserve a careful read. At the B7-only baseline (H_2 = 0%), SO_2 measured 0.25 ± 0.46 ppm; at H_2 = 5% and 10% it was 0.50 ± 0.53 ppm and 0.50 ± 0.58 ppm. Taken at face value those numbers would suggest SO_2 rising slightly with H_2 ratio, which is physically implausible since H_2 contains no sulfur. The catch is the spread: standard deviations of ±0.46–0.58 ppm exceed the means, so all SO_2 readings at H_2 ratios from 0 to 20% are statistically indistinguishable from zero at 95% confidence. The nominal "rise" at 5–10% is sensor noise near or below the SO_2 cell's detection limit (typically 1–2 ppm for the Testo 350), not a real emission. SO_2 remained below the detection limit (≈1–2 ppm) for all H_2 ratios; no trend can be resolved. Treat the SO_2 readings at H_2 ≤ 20% as qualitative only; do not use them for compliance reporting.

3.2 Steam Production Capacity

Adding hydrogen lifted steam output substantially (Fig. 2). At a 30% H_2/diesel energy ratio, steam output rose from 323.8 kg/hr (baseline) to 402.4 kg/hr (+24.3%) while the diesel feed sat between 20.2 and 20.5 kg/hr (CV = 0.57%). The added steam therefore reflects the additional energy input from H_2 rather than a more efficient conversion of the diesel itself; system thermal efficiency, by contrast, varies non-monotonically and declines at high H_2 ratios — peaking at 93.42% near 5% H_2 and falling to 87.45% at 30% (full discussion in Section 3.6).

The growth in steam output is monotonic and well captured by a quadratic regression (Eq. 6, valid for 0 ≤ r ≤ 0.30, R^2 = 0.986):

$$\dot{m}\_steam = -0.042r^2 + 3.793r + 326.5 \text{ (kg/hr, r in \%)} \qquad \text{(Eq. 6)}$$

The small negative quadratic term hints at a slight tail-off at higher H_2 ratios, probably as heat-transfer in the tube bundle becomes the limiting factor at higher total heat release.

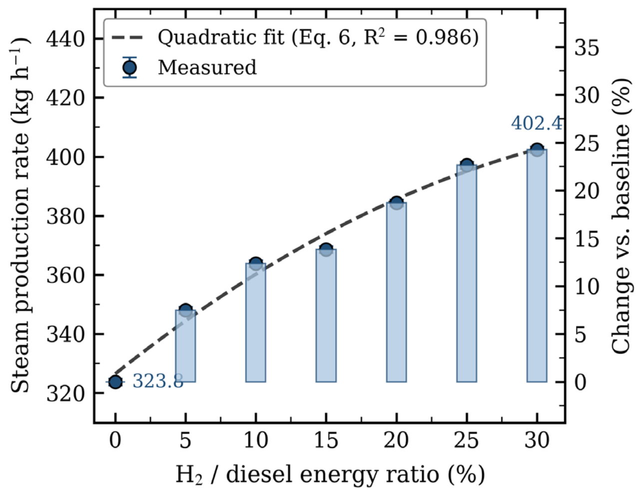

Fig. 2. Steam production rate (kg/hr) and percentage change vs. baseline as a function of H_2/diesel energy ratio. Error bars are ±95% confidence intervals (n = 4).

3.3 Effect on CO Emissions

Flue-gas CO fell monotonically from 106.5 ± 11.7 ppm at 0% H_2 to 28.5 ± 1.7 ppm at 30%, a 73.2% reduction (Fig. 3, upper left). The mechanism is well known: H_2 increases both local flame temperature and OH radical concentration, which speeds up CO oxidation through CO + OH → CO_2 + H. Our Dryer–Glassman CO burnout model (Dryer and Glassman, 1973) (calibration constant CO_scale = 0.414) reproduces the trend but slightly over-predicts CO, which is consistent with the simplifications of a single-zone reactor.

A 78-ppm reduction in CO (from 107 to 29 ppmv) is larger than what many conventional burner upgrades can deliver in practice. For facilities located in enclosed or semi-enclosed industrial estates, this translates into a tangible public-health benefit. A second-order polynomial regression fits the data well, valid for 0 ≤ r ≤ 0.30, with R^2 = 0.960:

$$CO = 0.0894r^2 - 4.931r + 100.6 \text{ (ppmv, r in \%)} \quad \text{(Eq. 7)}$$

The CO behavior fits the broad pattern in published H_2-enriched combustion work. Lan et al. (2024) reported stepwise CO reductions as the H_2 molar fraction grew in a natural-gas industrial heating furnace, comparable to the 73.2% drop we see

ISSN: 2252-4940/© xxx. The Author(s). Published by CBIORE

here, and the OH-mediated CO + OH → CO_2 + H pathway is the same. Wang et al. (2022) saw similar trends in a hydrogen-enriched gas-fired industrial boiler, and Glanville et al. (2022) reported comparable CO reduction trends in partially premixed combustion equipment fired on H_2/natural-gas blends. The OH-mediated route holds up across fuel types and burner geometries.

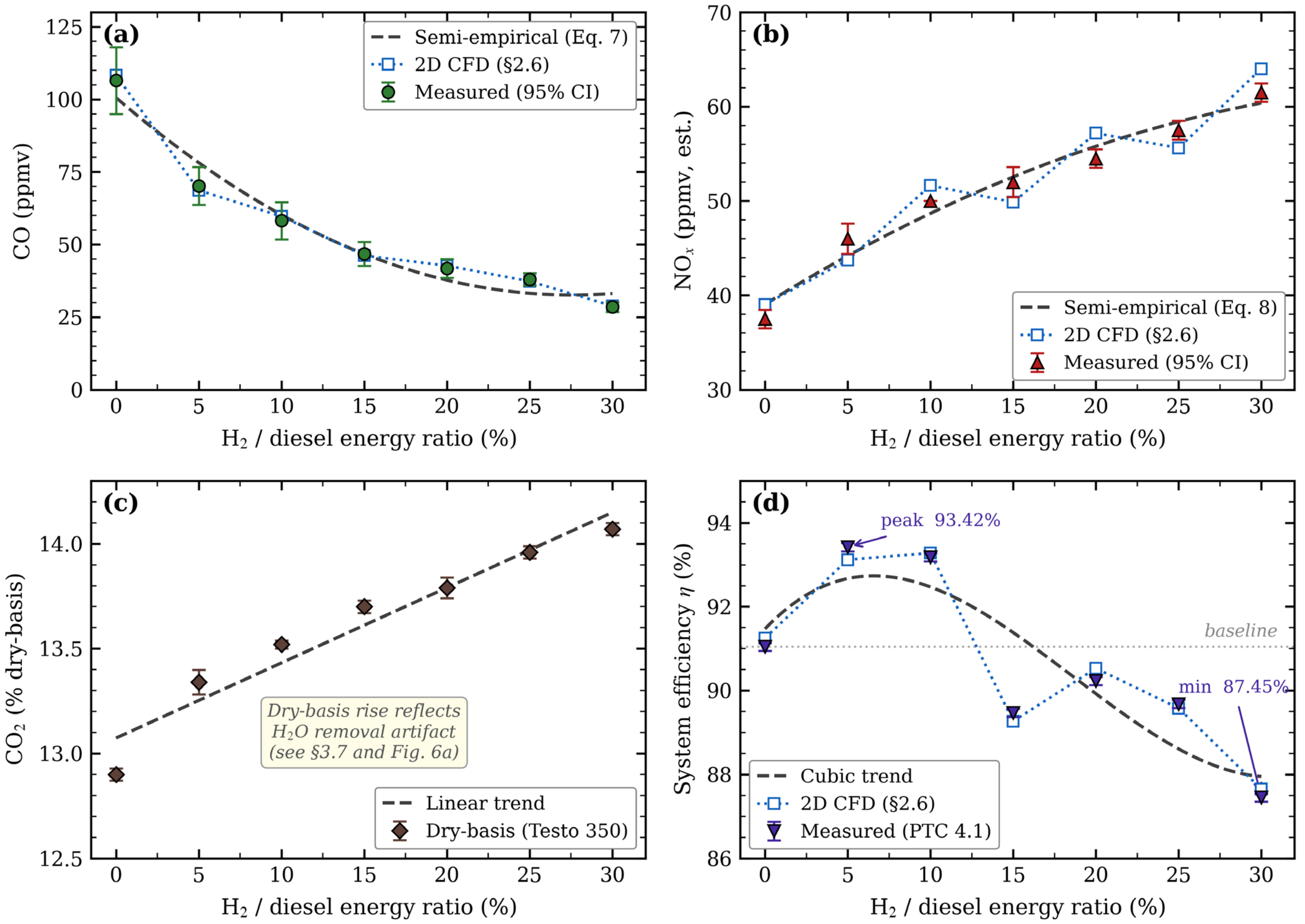

Fig. 3. Measured (markers) vs. modeled (lines) combustion parameters as a function of H_2/diesel energy ratio: (a) CO, (b) NO_x, (c) CO_2 dry-basis, (d) system efficiency (ASME PTC 4.1 Direct Method). Solid lines, semi-empirical correlations (Eqs. 7–9); dotted lines, 2D CFD predictions (§2.6). Error bars are 95% CI (n = 4). The dry-basis CO_2 rise in (c) is an H_2O-removal artifact (see Fig. 7a for wet-basis).

3.4 Effect on NO_x Emissions

Estimated NO_x rose with the H_2/diesel ratio (NO_2-derived; see §2.3). The value increased from 37.5 ± 1.0 ppm at the baseline to 61.5 ± 1.0 ppm at 30% H_2, a relative increase of 64.0% (Fig. 3, upper right). Repeatability also improved noticeably at the higher ratios. The coefficient of variation dropped from 17.8% at 0% H_2 to 2.3% at 30% H_2. This points to a more stable NO_x-formation environment, consistent with a hotter and more uniform flame once hydrogen is added to the fuel mix.

Qualitatively, the NO_x rise is no surprise for hydrogen-enriched hydrocarbon combustion. Several formation routes contribute to the observed levels (35–62 ppm): Zeldovich thermal NO_x, prompt NO_x (Fenimore) (Fenimore, 1971), and OH-mediated reactions. Their individual contributions cannot be teased apart from flue-gas measurements alone. The OH-enhancement coefficient β = 1.93 in Eq. 3 reproduces the observed trend and yields a reasonable model fit (MAPE 5.41%), but it does not establish the relative importance of any single pathway. Pulling those apart would require direct NO speciation or detailed kinetic modeling.

A near-linear NO_x rise with H_2 ratio (Eq. 8) might look at odds with the exponential temperature dependence of the Zeldovich thermal mechanism. Two effects explain the apparent linearity: the calculated adiabatic flame temperature only moves a little over the tested range, and the OH-mediated channel contributes a near-linear component that dominates over thermal-only NO_x. A second-order fit describes the trend, valid for $0 \le r \le 0.30$ ($R^2 = 0.969$).

A second-order fit captures the NO_x trend, valid for $0 \le r \le 0.30$ ($R^2 = 0.969$):

$$NO_x = -0.0126r^2 + 1.089r + 39.05 \text{ (ppmv, } r \text{ in \%)} \qquad \text{(Eq. 8)}$$

The magnitude of the NO_x rise lines up with published data on H_2-enriched combustion. Nemitallah et al. (2024) reported NO_x escalation across the full 0–100% H_2 range in a 207-MW retrofitted natural-gas-fired water-tube boiler, directly comparable to the ~64% increase estimated here at 30% H_2. They attributed the rise to higher adiabatic flame temperature and a larger OH pool, both of which are also at work in the B7–H_2 system. Wang and Yang (Wang and Yang, 2024) reviewed NO_x formation in turbulent combustion and reached the same conclusion: H_2 enrichment amplifies thermal NO_x via the Zeldovich pathway and via OH radicals. The absolute NO_x here (35–62 ppm) is well below typical gas-turbine values (80–150

ISSN: 2252-4940/© xxx. The Author(s). Published by CBIORE

ppm). That is expected: water-tube boilers run cooler and with longer residence times, conditions that favor CO burnout while suppressing peak thermal NO_x. A similar CO-down, NO_x-up trade-off has been documented at the engine scale in oxyhydrogen/producer-gas dual-fuel diesel engines, where multi-objective optimization of injection parameters has been needed to manage the trade-off at acceptable brake thermal efficiency (Nguyen et al., 2026). The convergence of this trade-off across boilers (the present work, 1 t/hr), industrial gas systems (Nemitallah et al., 2024), and IC engines (Nguyen et al., 2026) suggests the CO–NO_x exchange is a generic feature of H_2 co-firing rather than specific to any single combustion device.

Even at the highest tested ratio (30% H_2), absolute NO_x remained below 100 ppm, which is within the permissible limit for industrial boilers under the Thai factory chimney emission standard (Department of Industrial Works, 2022) and broadly in line with regulations across other Southeast Asian markets. As detailed in Section 2.3, the absolute NO_x values reported here should be regarded as semi-quantitative because the underlying NO_2 readings sit below the instrument's stated accuracy bound; only the upward trend is reliably resolved. The CO–NO_x trade-off in Fig. 4 makes the competing trends easy to read: CO drops sharply while NO_x rises, on a consistent trajectory as the H_2 fraction increases.

3.5 CO_2 Concentration and Dry-basis Measurement Effect

Dry-basis CO_2 readings rose with H_2 ratio, from 12.86 ± 0.11% at 0% to 14.06 ± 0.06% at 30% (Fig. 3, lower left). At first glance that runs against the stoichiometric prediction, which says dry-basis CO_2 should fall slightly because the H_2 flame brings additional N_2 (from extra excess air) into the products. The apparent rise is a measurement-basis artifact of desiccant-based electrochemical analyzers. As the H_2/diesel ratio climbs, the absolute water-vapor concentration in the flue gas climbs too (H_2 produces only H_2O), more water gets stripped per unit sample volume by the desiccant, and the residual dry-gas CO_2 mole fraction looks higher than it really is. The interpretation lines up with the high CO_2 repeatability (CV < 1%) and with the absence of any rise in CO_2 computed from a carbon balance.

Carbon accounting should therefore use the CO_2 intensity per kg of steam from the mass balance (Section 3.2), not the analyzer reading, since the analyzer reading reflects a measurement-basis effect rather than a real shift in combustion chemistry.

3.6 Boiler Thermal Efficiency and Flue-gas Temperature

Fig. 3 System efficiency (ASME PTC 4.1 Direct Method) shows a non-monotonic pattern with H_2 ratio (Fig. 3, lower right): from baseline 91.05%, rising to a peak of 93.42% at 5% H_2, then declining to 87.45% at 30% H_2 — a total drop of 3.60 pp from baseline (5.97 pp from peak). The early gain in the 5–10% range reflects more efficient combustion with hydrogen, with lower CO and improved burnout. The decline is non-monotonic, with local dips at 15% H_2 (89.47%) and 25% H_2 (89.68%) and a partial rebound at 20% (90.23%). These features are not measurement artifacts (efficiency CV < 0.07%); they arise from competing physical effects: (i) enhanced radical-pool activity and CO burnout that lift conversion efficiency, (ii) reduced soot loading and lower radiative heat transfer that depress it, and (iii) progressive supplemental-O_2 trimming that shifts local stoichiometry. A second-order polynomial captures only the broad downward trend ($R^2 \approx 0.70$); no closed-form efficiency correlation is reported because the non-monotonic dip-and-rebound pattern is not well described by a single polynomial.

Above 15% H_2, a different physical limit comes into play: as total heat release grows by ~30%, the convective heat-transfer area in the tube bundle becomes the bottleneck — flue-gas losses rise and the share of fuel energy converted into useful steam decreases. This is the main performance penalty of high-ratio H_2 co-firing in this boiler design, consistent with the slight leveling already seen in the steam-output curve (Eq. 6).

Flue-gas temperature rose by only 4.0 °C between baseline and 30% H_2 (193.2 ± 0.6 → 197.2 ± 0.1 °C). The 4 °C shift tracks the small rise in adiabatic flame temperature (2,363 → 2,387 K) and the increased thermal load on the tube bundle. A change that small confirms the heat-transfer surface is operating well within its thermal design envelope.

ISSN: 2252-4940/© xxx. The Author(s). Published by CBIORE

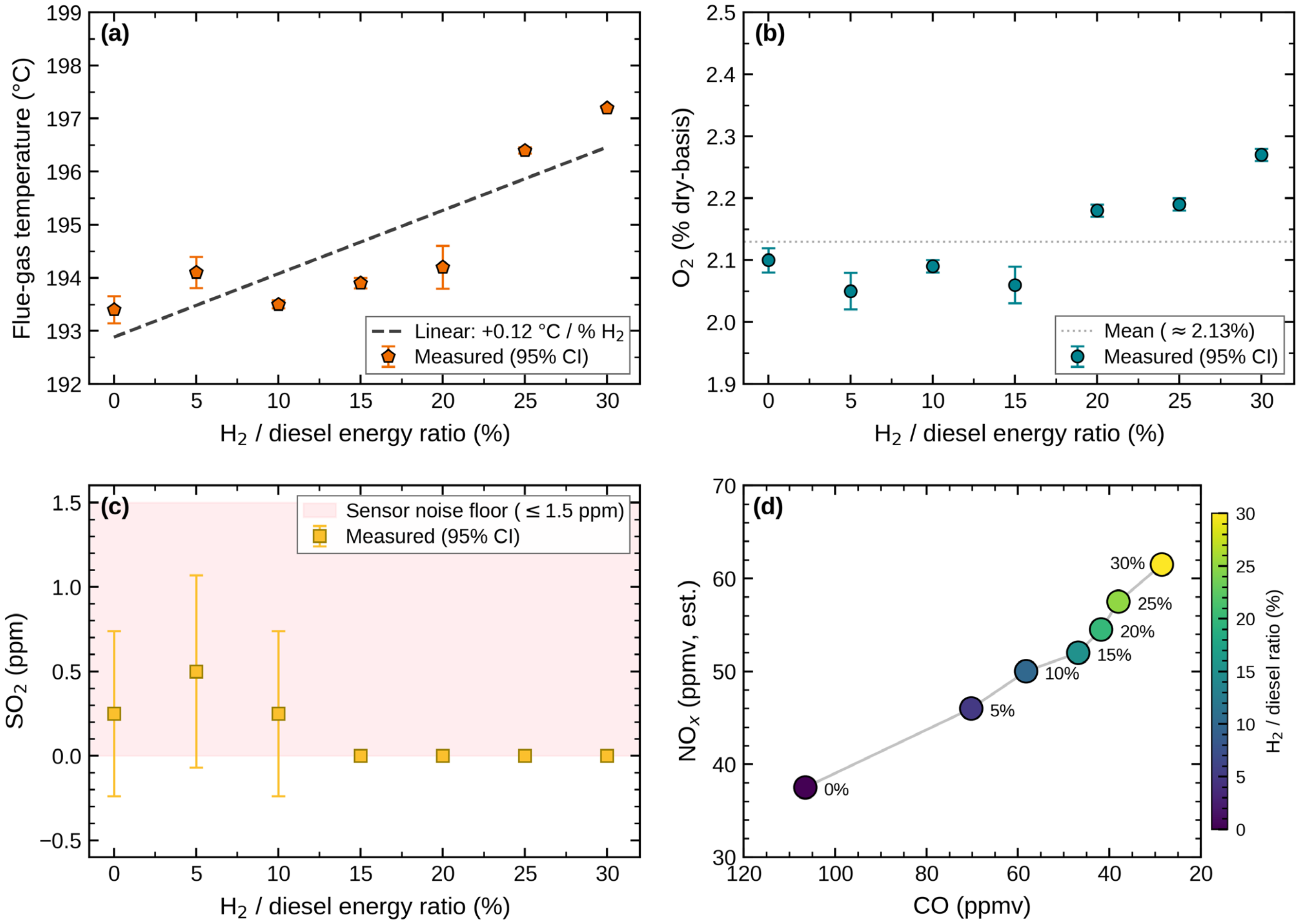

Fig. 4. Supplementary emission parameters: (a) flue-gas temperature, (b) O_2 concentration, (c) SO_2 emissions, (d) CO–NO_x trade-off diagram. Error bars = 95% CI.

3.7 Normalized Emission Trends and Regression Models

Fig. 5 plots the percentage change of every key parameter relative to baseline (0% H_2). CO and NO_x diverge sharply: CO drops roughly linearly at about −2.5 ppm per percent of added H_2, reaching −73.2% at 30%, while estimated NO_x climbs at about +0.9 ppm per percent, ending up ~+64.0% above baseline. Steam output and CO_2 intensity move in opposite, complementary directions (+24.3% and −20.1% at 30%, respectively). System efficiency (ASME PTC 4.1) follows a clear non-monotonic curve on the same plot: a slight gain of about +2.6% near 5–10% H_2, then a steady decline to −4.0% at 30% H_2. Flue-gas temperature is the only parameter that stays essentially flat across the H_2 range (within +2.1% of baseline). The figure makes the central trade-off visible at a glance: emissions and steam output respond strongly and monotonically to hydrogen enrichment, while system efficiency carries the bulk of the thermal performance penalty at the higher H_2 ratios.

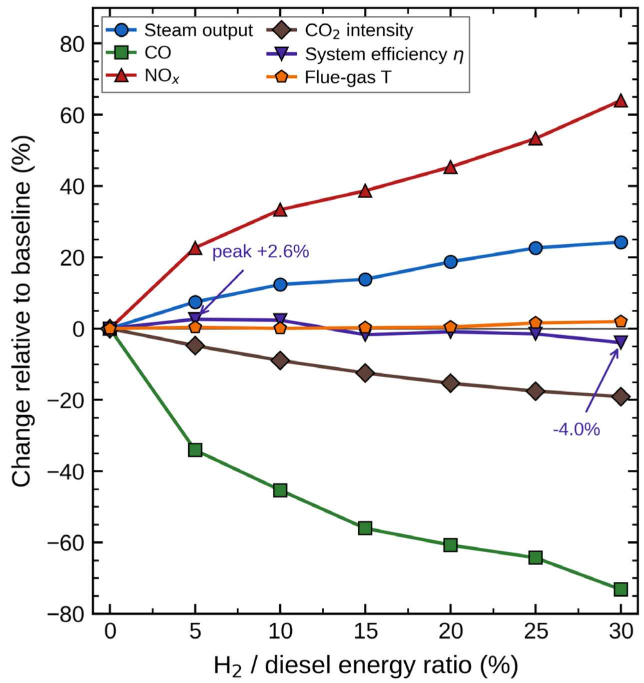

Fig. 5. Percentage change in steam output, CO, NO_x, CO_2 intensity, system efficiency, and flue-gas temperature relative to the B7-only baseline (0% H_2) as a function of H_2/diesel energy ratio. Symbols indicate measured means (n = 4).

ISSN: 2252-4940/© xxx. The Author(s). Published by CBIORE

Each second-order regression hits a strong fit ($R^2 \geq 0.960$), as shown in Fig. 6. The fitted correlations (Eqs. 6–9) can be used directly by operators to estimate emission performance and steam productivity at any H_2/diesel ratio in the tested range (0–30%).

$$CO_2 \ intensity = 0.026r^2 - 2.057r + 200.4 \ (g\ CO_2/kg\ steam,\ r\ in\ \%) \qquad (Eq.\ 9)$$

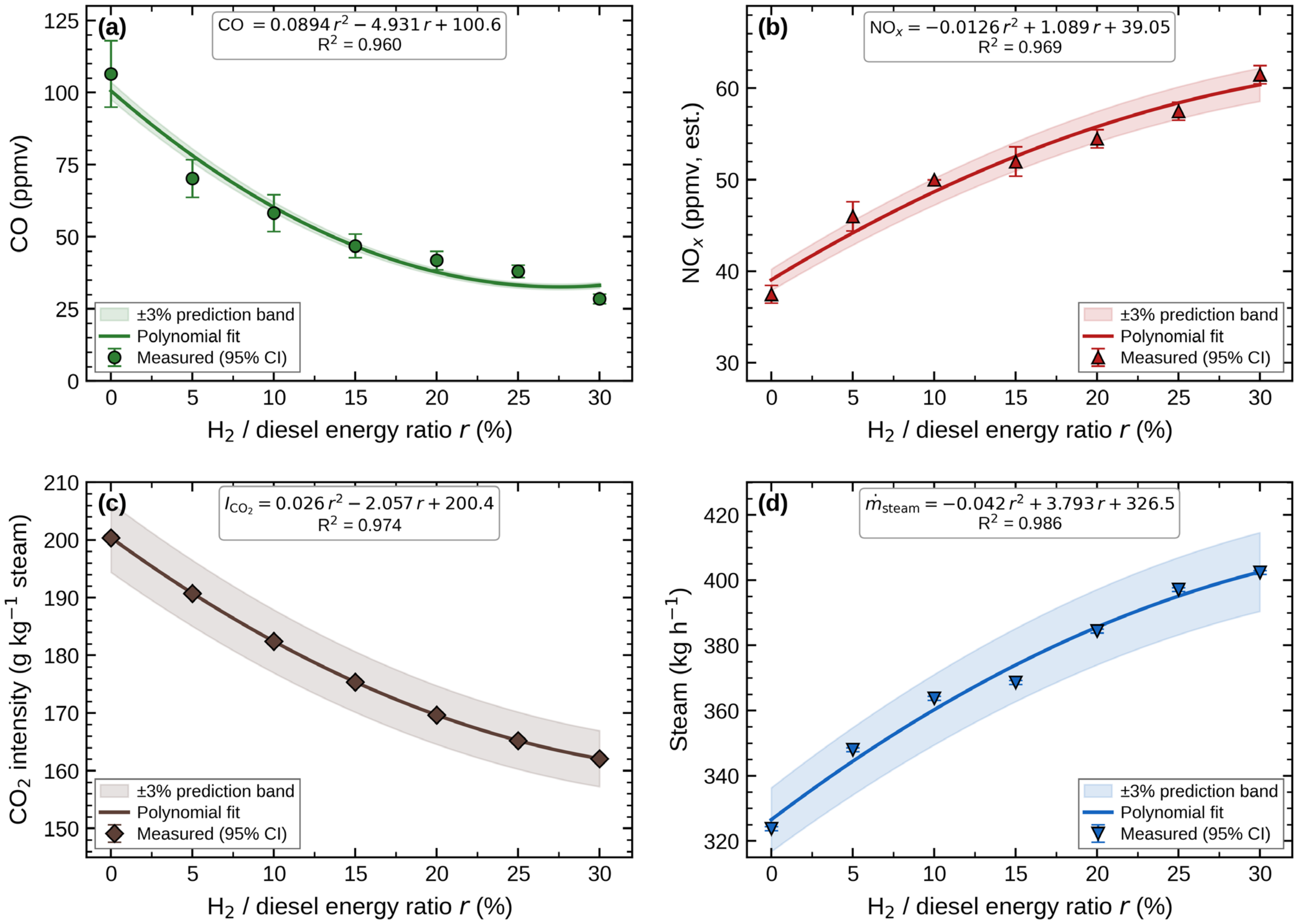

Fig. 6. Second-order polynomial regression fits for (a) CO, (b) NO_x, (c) CO_2 intensity, and (d) steam production rate vs. H_2/diesel energy ratio. Shaded bands indicate ±3% prediction interval.

3.8 Environmental Performance Assessment

Fig. 7 summarizes environmental performance under two complementary metrics. CO_2 intensity per kg of steam (Fig. 7a) drops from 202.5 g/kg (0% H_2) to 161.9 g/kg (30% H_2), a reduction of 40.6 g/kg or 20.1%. The improvement comes entirely from a larger denominator (more steam) rather than from any change in diesel use, which is what makes H_2 co-firing attractive on a per-unit-output basis without touching the primary fuel circuit.

When the same quantities are normalized to total fuel heat input (Fig. 7b), the CO index falls from 38.8 to 9.8 g/GJ (−74.7%) while the estimated NO_x index rises from 20.8 to 34.6 g/GJ (+66.3%).

ISSN: 2252-4940/© xxx. The Author(s). Published by CBIORE

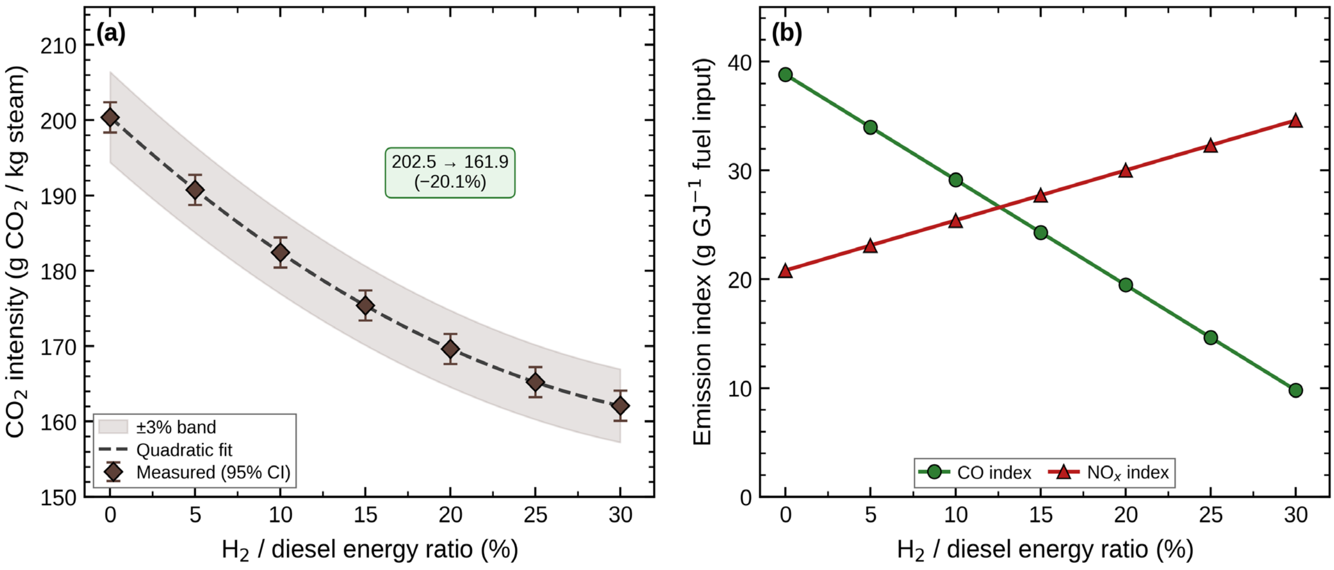

Fig. 7. Environmental analysis as a function of H_2/diesel energy ratio: (a) CO_2 intensity per kg steam (g CO_2/kg, with ±3% prediction band and Eq. 9 quadratic fit), (b) CO and NO_x emission indices normalized to total fuel-heat input (g/GJ).

3.9 Preliminary fuel-cost-only sensitivity analysis (excluding H_2 compression, storage, supplemental O_2, safety, and capital costs)

The economic case depends on both the H_2 supply price and the B7 diesel price, both of which are volatile. H_2 was supplied in bundles of sixteen 8.3 ft³ cylinders at 2,500 psi (≈172 bar), 8,525.76 THB per bundle, giving ~52.7 kg per bundle and an effective supply cost of ≈162 THB/kg (≈5.10 USD/kg). Thai industrial B7 averaged 43.7 THB/L (52.0 THB/kg). The baseline fuel cost is 3.27 THB per kg of steam. Capital, safety upgrades, H_2 storage, and maintenance fall outside this fuel-only analysis.

Fig. 8a plots the break-even H_2 price — the highest H_2 supply price keeping co-firing competitive with diesel-only — against the H_2/diesel ratio, parameterized over B7 prices of 25–60 THB/kg. At the current B7 price (52.0 THB/kg), the break-even H_2 price is ≈228 THB/kg at 5%, ≈185 THB/kg at 10%, and 120–140 THB/kg above 10%. Because the actual H_2 supply price is ≈162 THB/kg, co-firing is fuel-cost-favorable only up to ~12% H_2; above this, the marginal penalty grows to +3.2% at 15% and +6.4% at 30% relative to the diesel-only baseline. Fig. 8b extends the analysis into a 2-D cost-saving map at the actual H_2 price; the black contour marks the break-even boundary.

Looking further out, projected reductions in green H_2 cost (levelized costs in the 3–6 USD/kg range by 2030 under optimistic scenarios (IRENA, 2020)) could bring co-firing at moderate ratios (10–20%) close to parity with diesel-only operation, particularly if carbon pricing is applied to combustion emissions.

The same sensitivity, evaluated across four representative H_2 price scenarios (current 2026 prices; 2028 projection; 2030 IRENA target; long-term 2050), shows the fuel-cost-favorable window expanding from ≈12% H_2 at current prices to the full 0–30% range under 2030 IRENA assumptions, and becoming strongly cost-favorable in the long term. Per-scenario numerical penalties/savings are reported in the Supplementary Material.

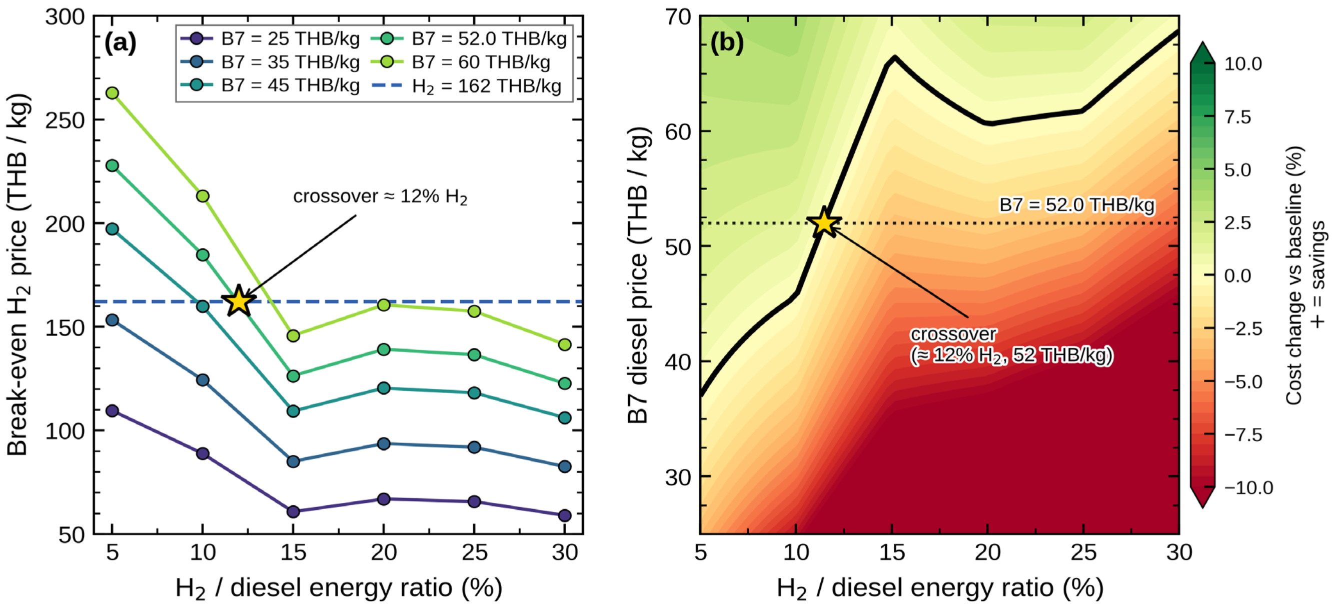

ISSN: 2252-4940/© xxx. The Author(s). Published by CBIORE

Fig. 8. Fuel-cost-only sensitivity analysis (capital, compression, storage, and safety costs excluded). (a) Break-even H_2 price vs. H_2/diesel energy ratio, parametric in B7 diesel price (25–60 THB/kg); the dashed navy line marks the actual H_2 supply price (162 THB/kg). (b) Two-dimensional cost-saving map (%) at the actual H_2 supply price; positive values indicate savings, the black contour marks break-even, and ★ marks the present operating point (≈12% H_2, B7 = 52 THB/kg). 2026 Thai market prices.

Beyond the cost lens, Fig. 9 summarizes overall boiler performance at four representative H_2/diesel energy ratios (0%, 10%, 20%, 30%) using a multi-parameter radar diagram, with each metric normalized to a 0–1 scale to visualize the steam-side gains, emission trade-offs, and efficiency penalty introduced in §3.1–3.8.

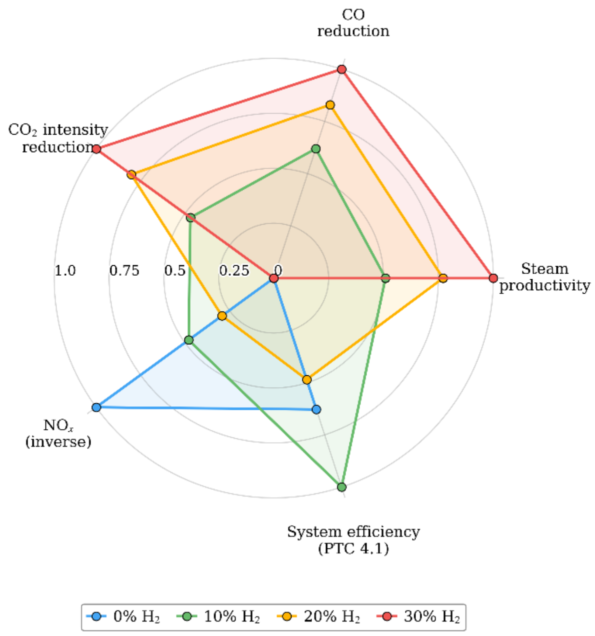

Fig. 9. Multi-parameter radar diagram comparing overall boiler performance at H_2/diesel energy ratios of 0%, 10%, 20%, and 30%. Each axis represents one performance metric — steam productivity, CO reduction, CO_2-intensity reduction, NO_x (inverse), and ASME PTC 4.1 system efficiency — normalized 0–1 (outer edge = most favorable across the four ratios).

3.10 Two-Dimensional CFD Results and Experimental Validation

Fig. 10 presents the 2D axisymmetric CFD field comparison in a vertical, down-firing orientation that mirrors the physical configuration. Temperature (top row), CO (middle row), and NO_x (bottom row) are shown at H_2 = 0%, 10%, 20%, and 30%. The flame anchors near the burner at all conditions; peak temperature shifts slightly upstream as H_2 increases. CO is concentrated in the upper combustion zone and decreases monotonically with H_2. NO_x remains low throughout but shows a clear localized peak near the burner that grows with H_2 ratio — consistent with thermal-NO_x amplification at higher peak temperatures.

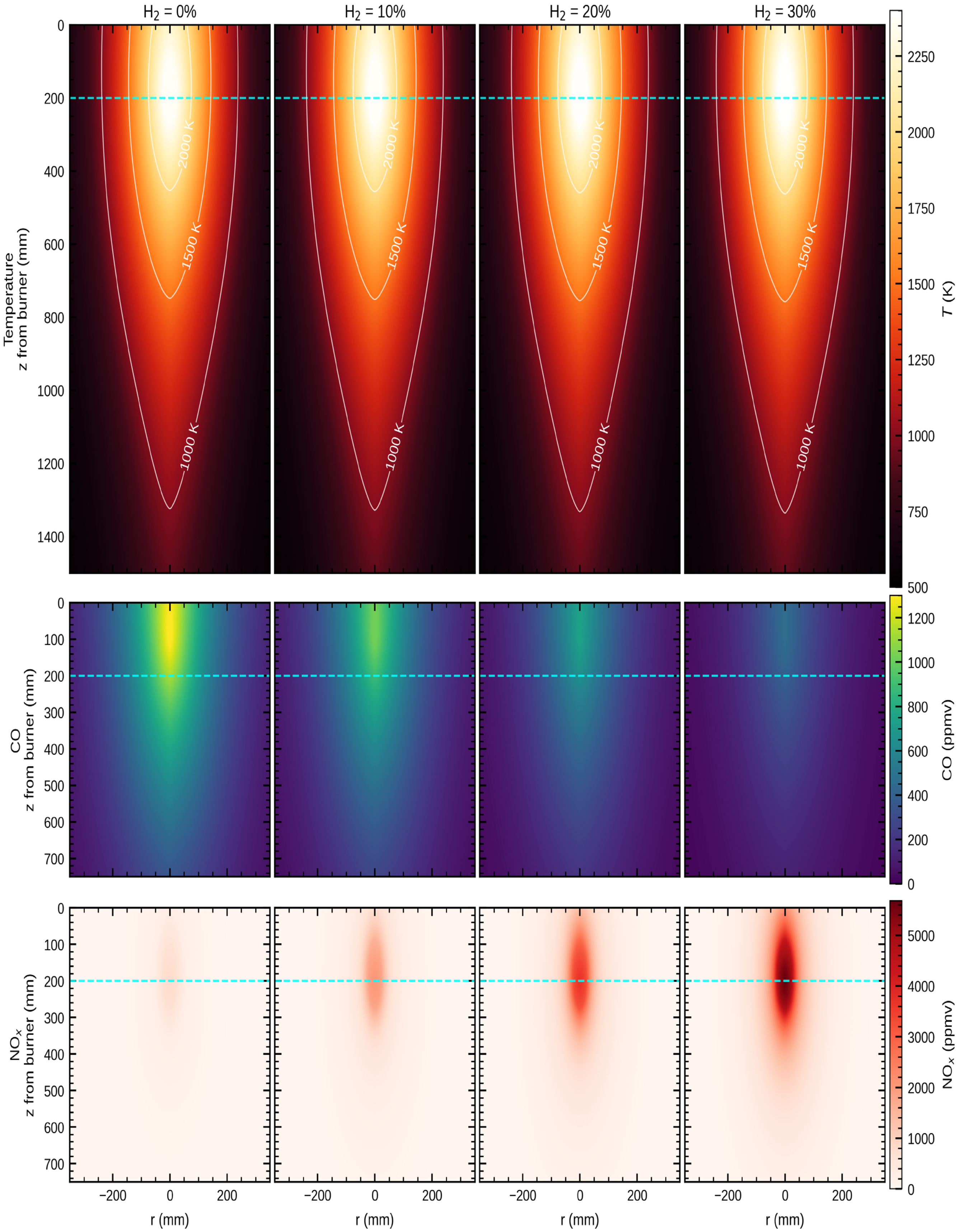

Fig. 10. 2D axisymmetric CFD field comparison in vertical, down-firing orientation: temperature (top row), CO concentration (middle row), and NO_x (bottom row) at H_2 = 0%, 10%, 20%, and 30% (columns left to right). All panels show r = -350 to +350 mm. The temperature row (top) covers the full chamber length (z = 0 to 1500 mm), while the CO and NO_x rows (middle, bottom) are cropped to z = 0 to 750 mm to highlight the active combustion zone. Dashed cyan lines mark the flame zone reference at z = 0.20 m. White isotherms in (a–d) indicate T = 1000, 1500, and 2000 K.

ISSN: 2252-4940/© xxx. The Author(s). Published by CBIORE

Fig. 11 shows parity charts comparing the CFD-predicted exit-plane concentrations against the experimental measurements for CO, NO_x, and flue-gas temperature across all seven H_2 ratios. The agreement is good in both direction and magnitude: CO MAPE 4.3%, NO_x MAPE 8.2%, with temperature predicted to within the experimental uncertainty (±3 °C). Errorbars on the experimental axis are one standard deviation (n = 4). Together, the Gaussian heat-release profile, the Dryer–Glassman CO burnout kinetics, and the Zeldovich–OH NO_x sub-model reproduce the measured exit-plane trends across the tested H_2 ratios. The slightly larger NO_x error at the lowest H_2 ratios (where Zeldovich dominates) reflects the well-known sensitivity of thermal NO_x to local temperature uncertainty.

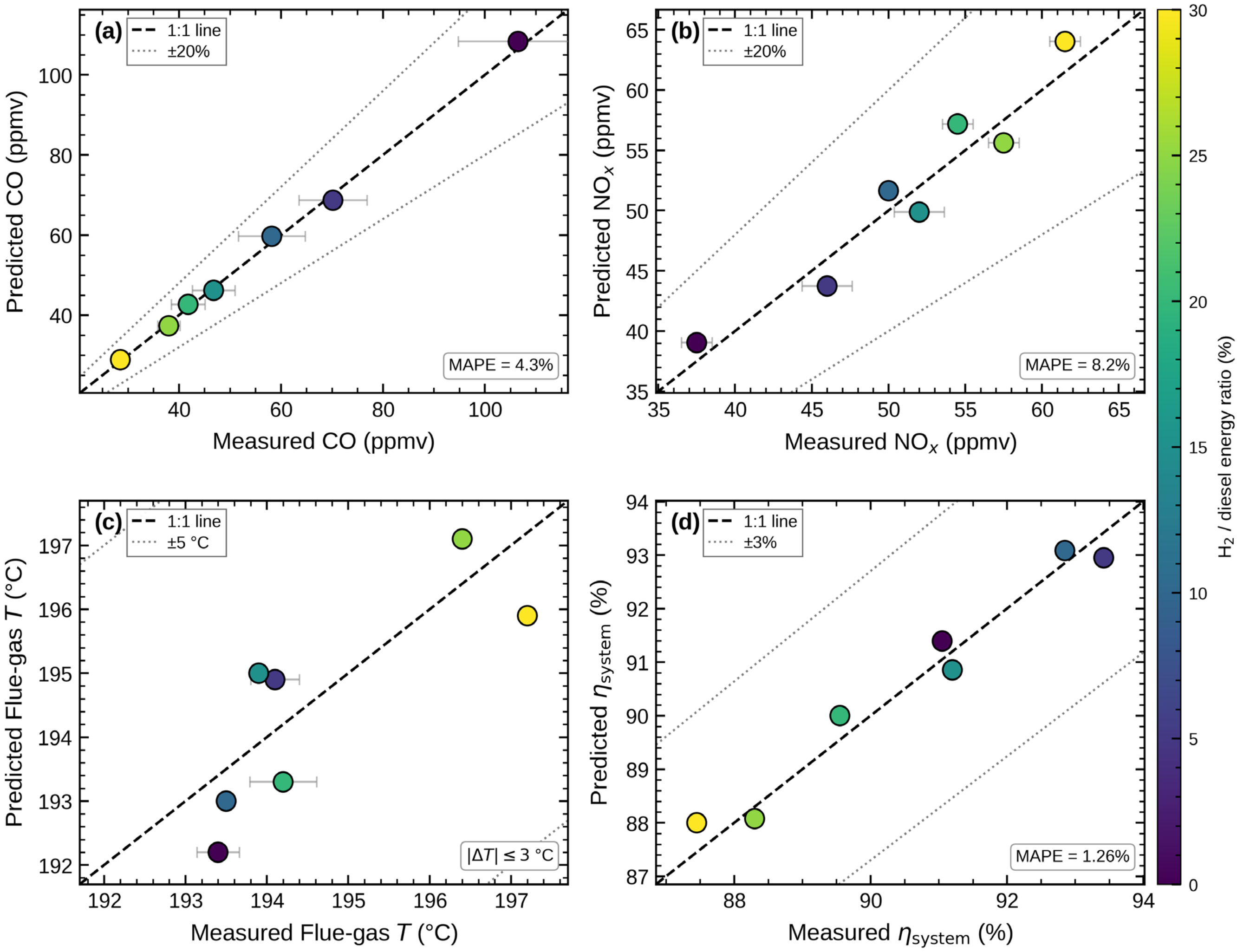

Fig. 11. Model vs. measurement parity charts: (a) CO (ppmv), (b) NO_x (ppmv), (c) flue-gas temperature (°C), (d) ASME PTC 4.1 system efficiency (%). Markers are colored by H_2/diesel energy ratio (0–30%); dashed line indicates 1:1 agreement; dotted lines bound ±20% (a–b), ±5 °C (c), and ±3% (d).

ISSN: 2252-4940/© xxx. The Author(s). Published by CBIORE

Comparison with prior CFD work in the same class (Xin et al.(2021), Sun et al.(2024)) shows broadly consistent qualitative trends — higher peak temperatures, faster heat release, and shifts in CO_2/H_2O partition — but quantitatively diverging NO_x predictions. The divergence is largely traceable to (i) the boundary conditions on excess air (fixed in Xin et al. and Sun et al., trimmed in the present study), and (ii) the NO_x-formation submodel (Xin et al. apply standard thermal-NO_x only; the present study uses Extended Zeldovich with OH-enhancement following (Glarborg et al., 2018) for the H_2-enriched regime, which captures the rise more accurately)

3.11 Study Limitations

Several limitations bound the present results: (i) all experiments at a single load (low-fire ~870 MJ/hr); medium-/full-fire response needs follow-up; (ii) NO_x estimated from NO_2 × 20 (see §2.3); (iii) H_2 flow metered by rotameter (±2% FS); r uncertainty ±3 pp of nominal; (iv) economic analysis covers fuel cost only — excludes capital, storage, safety interlocks, and maintenance; (v) results specific to Kawasaki 15750; generalization to other designs requires validation; (vi) ASME PTC 4.1 boundary excludes H_2 compression (~4% LHV) and supplemental O_2; (vii) supplemental O_2 raises flame temperature vs an air-only system, so absolute numbers cannot transfer directly to standard-air operation; (viii) 0 barg saturation operation; at typical 5–15 barg, heat-transfer and NO_x kinetics may differ.

The single-load constraint came from two practical issues: the available H_2 supply (≈52.7 kg per bundle at 2,500 psi in 16 × 8.3 ft³ cylinders) was not enough to sustain the H_2 flow rates needed for 20–30% energy substitution at medium- or high-fire loads, and the site safety clearance was granted specifically for the low-fire regime, pending a formal H_2 hazard assessment for higher-load operation. That kind of restriction is normal for early-stage H_2 co-firing retrofits, but it does mean these results should not be assumed to apply at higher loads without further validation.

Finally, the polynomial correlations (Eqs. 6–9) are valid only inside the tested 0–30% H_2/diesel range at low-fire. They should not be extrapolated past r = 30%, transferred to substantially different load conditions, or applied to boilers with different residence times or heat-transfer geometries without further experimental work. The regression coefficients are empirical fits to the Kawasaki 15750 at low-fire and are not mechanistic predictors.

The 20.1% point-of-combustion CO_2 reduction depends strongly on the H_2 production pathway. At 30% H_2, direct combustion CO_2 is 161.9 g/kg steam; adding upstream H_2-production CO_2 gives total lifecycle figures: gray hydrogen (~10 kg CO_2/kg H_2) → 238.7 g/kg (worse than the B7-only baseline of 202.5 g/kg); blue hydrogen (~1 kg CO_2/kg H_2) → 169.6 g/kg (preserves most of the benefit); green hydrogen (~0 kg CO_2/kg H_2) → 161.9 g/kg (full benefit). The direct-combustion benefit reported here is realized only when the H_2 source is green.

Beyond this single-boiler scale, broader industrial H_2 co-firing deployment faces system-level constraints (e.g., pipeline blending caps of 2–20 vol.% in current EU jurisdictions (Erdener et al., 2023)). The present low-fire campaign uses dedicated cylinder supply, so the regulatory/distribution constraints relevant to grid-blended H_2 apply only to scale-up scenarios beyond this study.

4. Conclusions

In the present work, the performance of hydrogen co-firing has been characterized in a commercial B7 diesel water-tube boiler over the H_2/diesel energy ratio range of 0 to 30%. The operating conditions of the campaign are representative of industrial practice. The experimental data have been interpreted with the help of a calibrated semi-empirical combustion model, together with a 2D axisymmetric CFD model. Both models were validated against the seven experimental test conditions. The main findings of the study are summarized below.

- **Steam productivity and efficiency. Steam output rose 24.3% at 30% H_2 (323.8 → 402.4 kg/hr) without additional diesel; system efficiency (ASME PTC 4.1) traced a non-monotonic curve from 91.05% baseline to a peak of 93.42% at 5% H_2 and down to 87.45% at 30% H_2 (Δη = −3.60 pp). The early gain reflects improved combustion completeness; the decline at higher ratios reflects heat-transfer-limited losses.**
- **Emissions trade-off. Alongside these steam-side gains, the emissions response was more nuanced: CO fell 73.2% (107 → 29 ppmv) via OH-mediated oxidation, while estimated NO_x rose ~64% (38 → 62 ppmv; NO_2-derived, §2.3) via thermal-NO_x amplification but remained below 100 ppm. CO_2 intensity per unit steam fell 20.1% (202.5 → 161.9 g/kg) on a point-of-combustion basis; the lifecycle benefit is realized only with green H_2 (see §3.11).**
- **Model performance. To capture this combined behavior in a tractable form, the semi-empirical model achieved MAPE of 5.41% on NO_x and 1.26% on boiler efficiency, useful as a screening tool where full 3D CFD is impractical.**
- **Economic outlook. Looking beyond the laboratory, fuel-cost-competitive operation is limited to ≈12% H_2 at 2026 Thai market prices; along the IRENA Green Hydrogen Cost Reduction trajectory toward 2030, the favorable window expands to the full 0–30% range tested (see §3.9).**

Within this single-boiler, single-load configuration, H_2 co-firing at 0–30% energy ratio is a viable retrofit option for B7 diesel water-tube boilers. Extension to other loads, boiler types, and fuel blends requires further experimental work. Priority follow-on items: CO–NO_x trade-off across multiple loads and excess-air ratios; direct NO speciation; full lifecycle techno-economic analysis; and longer operational durability testing.

Acknowledgements

This research was supported by the Rattanakosin College for Sustainable Energy and Environment, Rajamangala University of Technology Rattanakosin (RMUTR), which provided the Testo 350 flue-gas analyzer, and by Kation Power Co., Ltd., which provided the test boiler and experimental facilities. The authors thank all staff and personnel who helped during the experimental campaign.

Highlights

- First experimental H_2 co-firing data in a B7 diesel water-tube boiler (0–30%).
- Steam output rose 24.3% at 30% H_2 with no additional diesel consumption.

ISSN: 2252-4940

- CO_2 intensity fell 20.1%; CO −73.2%; estimated NO_x rose ~64% (semi-quantitative).
- System efficiency declined 3.6 pp (ASME PTC 4.1 Direct Method) at 30% H_2.
- Fuel-cost-favorable only up to ≈12% H_2 at 2026 Thai market prices.

CRediT Author Statement

Somkid Warasinchai: Conceptualization, Methodology, Software, Investigation, Writing – original draft. Pongsakorn Kachapongkun: Writing – review & editing, Supervision.

Funding

This research received no specific grant from any funding agency in the public, commercial, or not-for-profit sectors.

Declaration of Competing Interest

The authors declare that they have no known competing financial interests or personal relationships that could have appeared to influence the work reported in this paper.

Declaration of Generative AI and AI-assisted Technologies in the Writing Process

The authors used Claude (Anthropic) solely for language editing and improvement of readability of the written text in this manuscript, in accordance with IJRED's AI policy. All scientific content (experimental design, data collection, analysis, interpretation, and conclusions) was developed by the human authors, who take full responsibility for the integrity and accuracy of the manuscript. No AI tools were used to generate or alter any figures, images, or artwork. All references were independently verified by the authors against original sources.

Data Availability

The experimental data and model calibration files supporting the findings of this study are available from the corresponding author upon reasonable request.

References

AL-BAGHDADI, M. A. R. S., AHMED, S. S. & GHYADH, N. A. 2023. Three-dimensional CFD-solid mechanics analysis of the hydrogen internal combustion engine piston subjected to thermomechanical loads. *International Journal of Renewable Energy Development,* 12, 560-568.

ASME 2013. PTC 4.1 Steam Generator Units -- Power Test Code.

BOULAHLIB, M. S., MEDAERTS, F. & BOUKHALFA, M. A. 2021. Experimental study of a domestic boiler using hydrogen methane blend and fuel-rich staged combustion. *International Journal of Hydrogen Energy,* 46, 37628-37640.

CAPURSO, T., STEFANIZZI, M., TORRESI, M. & CAMPOREALE, S. M. 2022. Perspective of the role of hydrogen in the 21st century energy transition. *Energy Conversion and Management,* 251.

ÇENGEL, Y. A., BOLES, M. A. & KANOĞLU, M. 2019. *Thermodynamics: An Engineering Approach,* New York, NY, McGraw-Hill Education.

CORREA, S. M. 1993. A Review of NOxFormation Under Gas-Turbine Combustion Conditions. *Combustion Science and Technology,* 87, 329-362.

DEPARTMENT OF ENERGY BUSINESS 2020. Notification of the Department of Energy Business Re: Characteristics and Quality Specifications of Diesel Fuel, B.E. 2563 (2020). *Royal Thai Government Gazette.* Bangkok, Thailand: Ministry of Energy.

DEPARTMENT OF INDUSTRIAL WORKS 2022. Notification of Ministry of Industry regarding Factories to Install Special Device or Equipment for Reporting Air Pollution from Factory Chimney B.E. 2565 (2022). Bangkok: Ministry of Industry.

DEPARTMENT OF INDUSTRIAL WORKS 2024. Retrieved Data on Boiler Registration. Bangkok: Ministry of Industry.

DRYER, F. L. & GLASSMAN, I. High temperature oxidation of CO and CH4. Symposium (International) on Combustion, 1973. 987-1003.

ENERGY POLICY AND PLANNING OFFICE 2023. Annual Carbon Dioxide Emissions from the Energy Sector. Bangkok: Ministry of Energy.

ENERGY POLICY AND PLANNING OFFICE, ENERGY RESEARCH INSTITUTE, CHULALONGKORN UNIVERSITY & ENERGY RESEARCH AND DEVELOPMENT INSTITUTE, CHIANG MAI UNIVERSITY 2021. A Study Project on the Development of Hydrogen Production and Use to Promote Renewable Energy. Bangkok: Ministry of Energy.

EPRI 2020. Phase II Assessment of NO2/NOx Ratios at Fossil Fuel Power Plants. *EPRI Technical Update.* Palo Alto, California, USA: Electric Power Research Institute.

ERDENER, B. C., SERGI, B., GUERRA, O. J., LAZARO CHUECA, A., PAMBOUR, K., BRANCUCCI, C. & HODGE, B.-M. 2023. A review of technical and regulatory limits for hydrogen blending in natural gas pipelines. *International Journal of Hydrogen Energy,* 48, 5595-5617.

FENIMORE, C. P. Formation of nitric oxide in premixed hydrocarbon flames. Symposium (International) on Combustion, 1971. 373-380.

GERSENA, S., SLIMA, B., ZEIJLMAKERA, R., VAN ESSENA, M. & TICHELAARB, R. The development of a natural gas/hydrogen boiler system. The International Gas Union Research Conference, 2020. 1-8.

GLANVILLE, P., FRIDLYAND, A., SUTHERLAND, B., LISZKA, M., ZHAO, Y., BINGHAM, L. & JORGENSEN, K. 2022. Impact of Hydrogen/Natural Gas Blends on Partially Premixed Combustion Equipment: NOx Emission and Operational Performance. *Energies,* 15.

GLARBORG, P., MILLER, J. A., RUSCIC, B. & KLIPPENSTEIN, S. J. 2018. Modeling nitrogen chemistry in combustion. *Progress in Energy and Combustion Science,* 67, 31-68.

HOSSEINI, S. H., TSOLAKIS, A., ALAGUMALAI, A., MAHIAN, O., LAM, S. S., PAN, J., PENG, W., TABATABAEI, M. & AGHBASHLO, M. 2023. Use of hydrogen in dual-fuel diesel engines. *Progress in Energy and Combustion Science,* 98.

IEA 2023. Energy Technology Perspectives 2023. Paris: International Energy Agency (IEA).

IEA 2024. Southeast Asia Energy Outlook 2024. Paris: International Energy Agency (IEA).

IRENA 2020. *Green Hydrogen Cost Reduction: Scaling up Electrolysers to Meet the 1.5^{O}C Climate Goal,* Abu Dhabi, International Renewable Energy Agency.

IRENA 2024. Renewable energy statistics 2024. Abu Dhabi: International Renewable Energy Agency (IRENA).

JAYABAL, R. & SIVANRAJU, R. 2025. Environmental and Emission Analysis of Biodiesel/Bioethanol/Nanoparticles Blends With Hydrogen Addition in Diesel Engine. *Energy Science & Engineering,* 13, 4024-4031.

KHIRAIYA, K., RAMANA, P. V., PANCHAL, H., SADASIVUNI, K. K., DORANEHGARD, M. H. & KHALID, M. 2021. Diesel-fired boiler performance and emissions measurements using a combination of diesel and palm biodiesel. *Case Studies in Thermal Engineering,* 27.

LAGET, H., GRIEBEL, P., GOOREN, L., HAMPP, F., JOURET, N. & LAMMEL, O. 2023. Demonstration of Natural Gas and Hydrogen Cocombustion in an Industrial Gas Turbine. *Journal of Engineering for Gas Turbines and Power,* 145, 041007.

LAN, Y., WANG, Z., XU, J. & YI, W. 2024. The Impact of Hydrogen on Flame Characteristics and Pollutant Emissions in Natural Gas Industrial Combustion Systems. *Energies,* 17.

LAW, C. 2006. Combustion Physics.-Cambridge Univ. Press, N. J.

LIN, K.-W. & WU, H.-W. 2023. Emissions and energy/exergy efficiency in an industrial boiler with biodiesel and other fuels. *Case Studies in Thermal Engineering,* 50.

LONG HUYNH, D. N., NGUYEN, T. H., NGUYEN, D. C., VO, A. V., NGUYEN, D. T., NGUYEN, V. Q. & LE, H. C. 2024. Using hydrogen as potential fuel for internal combustion engines: A

ISSN: 2252-4940

comprehensive assessment. *International Journal of Renewable Energy Development,* 14**,** 83-103.

NASA 1997. Safety Standard for Hydrogen and Hydrogen Systems: Guidelines for Hydrogen System Design, Materials Selection, Operations, Storage, and Transportation. Washington, DC: NASA Office of Safety and Mission Assurance.

NEMITALLAH, M. A., ALIYU, M., HAMDY, M. & HABIB, M. A. 2024. Retrofitting Natural Gas–Fired Boiler for Hydrogen Combustion: Operational Performance and NOx Emissions. *Journal of Energy Resources Technology,* 146**,** 1-12.

NGUYEN, D., NGUYEN, L. H., NGUYEN, D. T., CHUNG, N. & TRUONG, T. H. 2026. Integrated multi-objective optimization of fuel injection and engine strategy in oxyhydrogen/producer gas-powered dual-fuel diesel engine. *International Journal of Renewable Energy Development,* 15**,** 147-159.

PAN, H., GENG, S., YANG, H., ZHANG, G., BIAN, H. & LIU, Y. 2023. Influence of H2 blending on NOx production in natural gas combustion: Mechanism comparison and reaction routes. *International Journal of Hydrogen Energy,* 48**,** 784-797.

PERIYATHAMBI, V., EZHUMALAI, M., GOVINDASAMY, M., DHAIRIYASAMY, R., VARSHNEY, D. & SINGH, S. 2025. Balancing Efficiency and Emissions: A Study on Biodiesel-Hydrogen Dual-Fuel Engine Performance Under Varying Injection Timings. *Engineering Reports,* 7**,** e70174.

SCHWARZ, S., DAURER, G., GABER, C., DEMUTH, M., PRIELER, R. & HOCHENAUER, C. 2024. Experimental investigation of the combustion characteristics in oxy-fuel combustion of hydrogen-enriched natural gas on a semi-industrial scale. *International Journal of Hydrogen Energy,* 49**,** 323-337.

STULTZ, S. C. & KITTO, J. B. 2005. *Steam: Its Generation and Use,* Barberton, OH, The Babcock & Wilcox Company.

SUN, C., WANG, T., WANG, P., ZHANG, Y., CUI, C., LU, Y., LIU, W., ZHANG, Y. & ZHANG, Y. 2024. Numerical Simulation and Field Experimental Study of Combustion Characteristics of Hydrogen-Enriched Natural Gas. *Processes* [Online], 12.

TURNS, S. R. 1996. *Introduction to combustion*, McGraw-Hill Companies New York, NY, USA.

WANG, T., ZHANG, H., ZHANG, Y., WANG, H., LYU, J. & YUE, G. 2022. Efficiency and emissions of gas-fired industrial boiler fueled with hydrogen-enriched nature gas: A case study of 108 t/h steam boiler. *International Journal of Hydrogen Energy,* 47**,** 28188-28203.

WANG, Z. & YANG, X. 2024. NOx Formation Mechanism and Emission Prediction in Turbulent Combustion: A Review. *Applied Sciences,* 14.

WARASINCHAI, S. & KACHAPONGKUN, P. 2026. Effects of Hydrogen Gas Addition on Combustion Efficiency and Pollutant Emissions in a 1-ton/hour Diesel B7 Boiler [in Thai]. *The Journal of Industrial Technology***,** in press.

XIN, Y., WANG, K., ZHANG, Y., ZENG, F., HE, X., TAKYI, S. A. & TONTIWACHWUTHIKUL, P. 2021. Numerical Simulation of Combustion of Natural Gas Mixed with Hydrogen in Gas Boilers. *Energies,* 14.

ISSN: 2252-4940 / © 2026. The Author(s). Published by CBIORE